

**Shape and Stress Analysis
of Symmetric CRTS Reflectors**

C.Y. Lai, Z. You and S. Pellegrino
CUED/D-STRUCT/TR170(revised)

European Space Agency Contractor Report

The work presented in this report was carried out under an ESA contract.

Responsibility for its contents resides with the authors.

ESA Study Manager: W.J. Rits

ESTEC Contract no. 11936/96/NL/FG

Release date: 15 December 1997

Revised edition: 15 March 2001

Abstract

The *Collapsible Rib-Tensioned Surface (CRTS)* reflector is a new concept for multipurpose deployable membrane reflectors that is being developed by the European Space Agency. It is based on the inherent geometrical stability of a doubly-curved membrane with high in-plane stiffness, maintained in a state of tension by a series of flexible ribs. The shape of a CRTS reflector is not uniquely determined. It results from a compromise between the best possible approximation to a paraboloidal surface and a nearly-uniform bi-axial state of prestress of the membrane surface, to avoid the formation of wrinkles.

This report investigates the shape and stress distribution of CRTS reflectors, both analytically and experimentally. The analytical part of the study establishes a methodology for the preliminary design of symmetric reflectors of given aperture, focal length, and target rms error. The concepts of a *reference surface* and of an *equilibrium surface* are introduced, and algorithms are developed to compute these surfaces and their associated rms error. Then, the cutting pattern for making the membrane is computed and the rms error of the actual surface is predicted. Estimates are made of the rms error of CRTS reflectors with apertures of 1, 3, 5, and 10 m, with 6, 12, and 24 ribs.

The experimental part of the study compares the measurements of prestress and shape in a one-sixth sector of a 1 m diameter reflector with 6 ribs, with predictions obtained from the computational study.

Contents

1	Introduction	1
1.1	CRTS Reflectors	1
1.2	Reference Surface	2
1.3	Equilibrium Surface	5
1.4	Design Methodology	7
1.5	Layout of this Report	7
2	Computational Method	8
2.1	Background	8
2.2	Approach	9
2.3	Mesh and Boundary Conditions	9
2.4	Computation of Equilibrium Surface	11
2.4.1	Procedure	15
2.5	Computation of Cutting Pattern	15
2.6	Elastic Analysis	17
2.7	Rib Profile	21
3	Computational Results	22
3.1	Introduction	22
3.2	Analysis of 1 m Reflector with 6 Ribs	22
3.2.1	Equilibrium surface	22
3.2.2	Membrane cutting pattern and elastic analysis	27
3.2.3	Rib profile	30
3.3	Analysis of Larger Reflectors	30
4	Experiment Preparation	34
4.1	Test Article	34
4.1.1	Membrane	35
4.1.2	Ribs	35
4.1.3	Hub	36
4.1.4	Connections	38
4.2	Measurement Methods	39
4.2.1	Strain measurements	39
4.2.2	Shape measurements	41
4.3	Material Properties	41
4.3.1	Membrane	41
4.3.2	Ribs	45

4.3.3	Adhesive tape	45
5	Experimental Results	46
5.1	Prestress Adjustment	46
5.2	Shape Measurement	48
6	Conclusion	51
6.1	Discussion	51
6.2	Recommendations	52
6.3	Acknowledgements	52
A	Computation of rms error	53
B	Manufacturing Drawings	56

List of Tables

1.1	Reference surface, rms error of CRTS reflectors with $F/D=0.78$	4
3.1	Nodal loads on a rib.	30
3.2	Number of nodes and elements in each mesh.	31
3.3	Modelling error.	31
3.4	Unweighted rms errors of reflectors with $F/D = 0.78$ [mm].	32
3.5	Area-weighted rms errors of reflectors with $F/D = 0.78$	33
4.1	Properties of Kevlar-reinforced Kapton foil	35
4.2	Rib properties.	37
4.3	Position of strain gauges in the coordinate system of Fig. 4.8.	40
4.4	Elastic moduli of Kevlar-reinforced Kapton foil (Oerlikon-Contraves 1993).	42
4.5	Elastic moduli of membrane.	42
5.1	Strain measurements [micro-strains].	47
5.2	Strain adjustment sequence [micro-strains]	48
5.3	Coordinates of target points.	49

List of Figures

1.1	Schematic view of CRTS reflector with 10 ribs.	1
1.2	A possible packaging scheme.	3
1.3	Reference surface (a) complete view; (b) one gore only; (c) one gore, flattened.	4
1.4	Error of reference surface of reflector with $D=1$, $F=0.78$, and $n=6$ [mm].	5
1.5	Shell element.	6
2.1	Initial mesh, plan view.	10
2.2	Cable networks	11
2.3	Triangular element.	13
2.4	Surface projection.	18
2.5	Configurations of an elastic membrane element	19
2.6	Force components on a rib.	21
3.1	Initial mesh.	23
3.2	Equilibrium surface.	24
3.3	Equilibrium surface, predicted stress distribution.	25
3.4	Equilibrium surface, predicted stress distribution.	26
3.5	Equilibrium surface, direction and magnitude of principal stresses.	27
3.6	Cutting pattern for half gore (dimensions in metres).	28
3.7	Error of actual surface	28
3.8	Stress distribution in actual surface (Kevlar-reinforced membrane).	29
3.9	Stress distribution in actual surface (0.02 mm thick Kapton membrane).	29
3.10	Unstressed rib shape.	31
4.1	Schematic top view of test article.	34
4.2	Mould on which the gores are bonded.	36
4.3	Rib cross-section.	37
4.4	Moment/rotation relationship for a rib.	37
4.5	Cross-section of rib sliding block.	38
4.6	End plate.	38
4.7	Edge cable connector.	39
4.8	Layout of strain gauges and numbering of adjustments.	40
4.9	Schematic layout of tension test on membrane strip.	43
4.10	Tension tests on membrane strips.	44
5.1	Target points on the surface model.	48
A.1	Best-fit paraboloid	54

B.1	Hub element; dimensions in millimetres.	56
B.2	Plywood base plate; dimensions in millimetres.	57
B.3	Plywood side plate; dimensions in millimetres.	57
B.4	Rib stop; dimensions in millimetres.	58
B.5	End plate; dimensions in millimetres.	58

Chapter 1

Introduction

1.1 CRTS Reflectors

Large deployable reflectors are being used increasingly for satellite communication, radioastronomy and radar surveillance. The requirement for large apertures that can be compactly packaged for launch and reliably deployed in orbit, to achieve their intended configuration precisely, has spurred extensive new research worldwide.

A new concept for multipurpose deployable membrane reflector is being developed by the European Space Agency (ESA 1992; Rits 1996). This new concept is known as the *Collapsible Rib-Tensioned Surface (CRTS)* reflector. It is based on the inherent geometrical stability of a doubly-curved membrane with high in-plane stiffness, which is maintained in a state of tension by a series of flexible ribs.

A CRTS reflector consists of three main parts. A central expandable hub, a series of thin-walled foldable ribs connected radially to the hub, and a precision shaped membrane that is supported and tensioned by the ribs. A schematic diagram of the reflector is shown in Fig. 1.1.

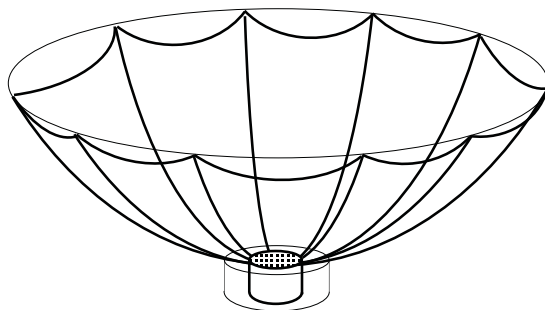


Figure 1.1: Schematic view of CRTS reflector with 10 ribs.

During deployment the radius of the hub is at its minimum, so that the ribs can

deploy the membrane without having to prestress it at the same time. Once the membrane has been fully deployed, the hub is expanded, thus pushing the ribs outwards. This has the effect of applying a state of prestress to the membrane, thus setting it into its intended shape. In the case of a symmetric reflector, the membrane consists of identical, flat gores bonded together along their curved edges. When the reflector is deployed, each gore takes approximately the shape of a singly-curved, cylindrical surface. Therefore, the overall shape of the reflector is not an exact paraboloid, but only an approximation to it whose accuracy improves as the number of gores is increased.

The membrane is fully attached to the ribs only at the outer edge. Elsewhere, a small relative motion between them is allowed; this is particularly important if a uniform distribution of prestress is to be achieved. In a small scale model of a CRTS reflector made in our laboratory a few years ago (You and Pellegrino 1994), each rib was mounted inside a sleeve formed by looping the membrane above the seam between two adjacent gores, with the convex side facing towards the focus of the reflector. However, a better shape accuracy can be achieved if the ribs are mounted behind the reflective surface.

Each rib consists of a thin, slender metal blade with curved cross-section. A key feature of this structural element is that it is continuous, i.e. it contains no mechanical hinges or other folding devices, and yet it can be folded elastically in many different ways. For example, it can be rolled up into a coil with a radius approximately equal to the transverse radius of curvature of the cross-section, or it can be folded by forming a series of up-and-down, discrete elastic folds. The deployment behaviour of this type of rib structure has already been investigated extensively, see Fischer (1994) for a detailed study of the moment-rotation response of straight ribs, and Seffen and Pellegrino (1999) for models of their deployment dynamics. The behaviour of curved ribs, which is also being investigated as a part of this project, is described in a separate report (Seffen, You and Pellegrino 1997).

A previous investigation of possible packaging schemes for CRTS reflectors (You and Pellegrino 1994) has identified three alternatives: (i) inward rolling of the ribs with radial folding of the membrane; (ii) zig-zag folding of the ribs with radial folding of the membrane; (iii) wrapping of ribs and membrane around the hub. Figure 1.2 shows the second scheme, which emerged as the preferred option at the end of that preliminary study.

1.2 Reference Surface

In a paraboloidal surface the principal curvatures κ_1 and κ_2 have equal signs, and hence the gaussian curvature is positive everywhere

$$\kappa_1 \kappa_2 > 0$$

However, the gores of a CRTS reflector have negative gaussian curvature (this will be shown in the next section) and hence it is inherent in this concept that the reflective surface can never form a perfect paraboloid.

A preliminary estimate of the rms error of a CRTS reflector, from which the antenna gain can be estimated as shown in Appendix A, can be obtained from simple geometric considerations, as follows.

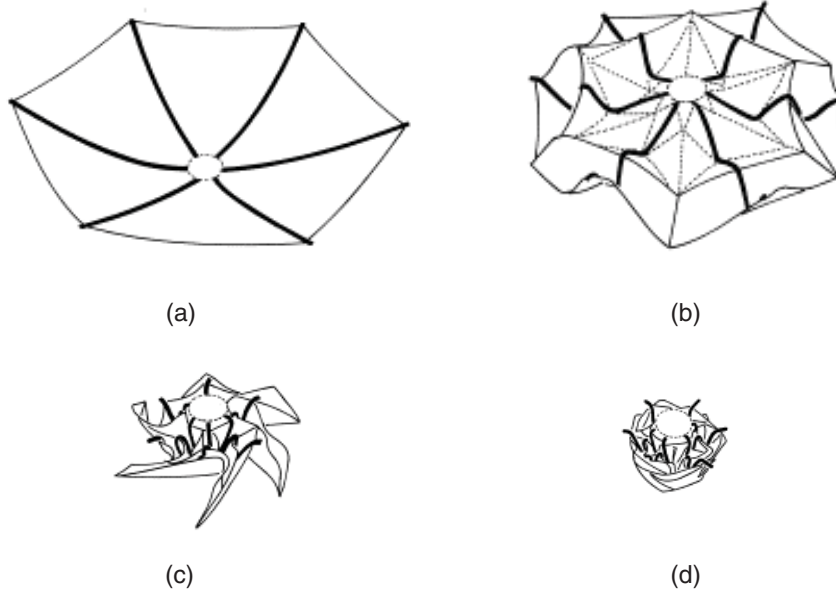


Figure 1.2: A possible packaging scheme.

It will be assumed that each gore has the shape of a cylindrical surface, Fig. 1.3a, and hence it is a developable surface with $\kappa_1 = 0$, whose intersections with the radial planes that bound that gore coincide with the parabolas obtained by intersecting the desired paraboloid with the same planes, Fig. 1.3b. The outer edge of the gore is a straight line. This surface is not practically achievable, but it provides a convenient geometric reference, and will be called the *reference surface*.

The rms errors of the reference surface of CRTS reflectors with $F/D = 0.78$, but different values of D and different numbers of ribs, n , were computed using 250 – 300 target points per gore. Their values are listed in Table 1.1, where the two columns correspond to the least squares solution of Eq. A.6 —without considering the surface area associated with each target point— and a more refined solution using weighted least squares. It can be seen that the area weighting makes little difference, as the targets were fairly evenly distributed.

Figure 1.4a shows a contour plot of the z -error between the reference surface and the best fit paraboloid for a gore of a reflector with $F = 0.78$ m, $D = 1$ m and $n = 6$. Figure 1.3b shows a contour plot of the z -error between the equilibrium surface, see Section 1.3, and the best fit paraboloid, for the same reflector.

Finally, it should be noticed that the rms error of the reference surface is always an underestimate of the rms error that is achievable if biaxial prestress of the membrane is required. For the range of configurations that have been considered in this study, the achievable rms error is typically 50% worse than the values given in Table 1.1, as will be shown in Section 3.3.

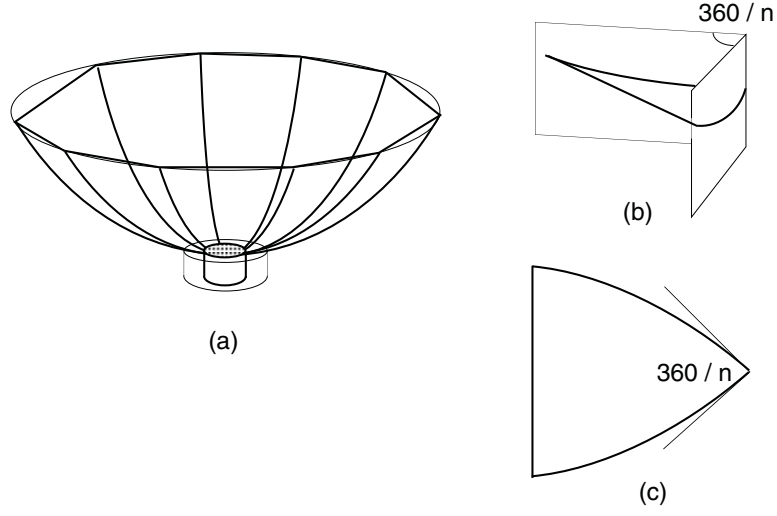


Figure 1.3: Reference surface (a) complete view; (b) one gore only; (c) one gore, flattened.

D [m]	n	rms error [mm]	weighted rms error [mm]
1	6	3.3	3.0
	12	1.0	0.9
	24	0.3	0.2
3	6	9.5	8.8
	12	2.8	2.6
	24	0.7	0.7
5	6	15.6	14.7
	12	4.7	4.3
	24	1.2	1.1
10	6	31.1	29.3
	12	9.3	8.6
	24	2.4	2.2

Table 1.1: Reference surface, rms error of CRTS reflectors with $F/D=0.78$.

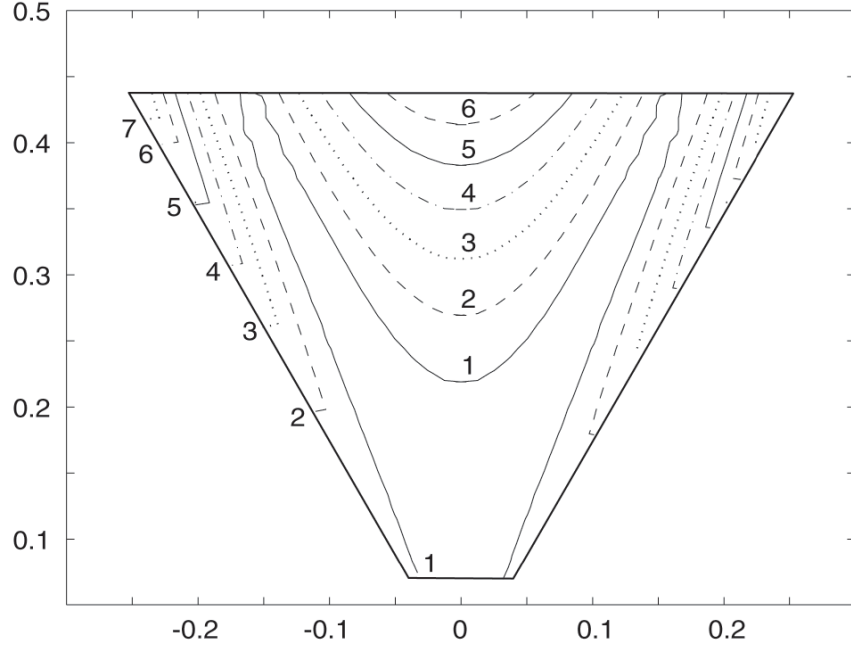


Figure 1.4: Error of reference surface of reflector with $D=1$, $F=0.78$, and $n=6$ [mm].

1.3 Equilibrium Surface

The shape of a CRTS reflector is not uniquely determined. It results from a compromise between two conflicting requirements. First, obtaining the best possible approximation to a paraboloidal surface; second, being able to apply a uniform bi-axial state of prestress, which makes it possible to avoid the formation of wrinkles in the membrane. (A third, practical requirement that will be considered in the next chapter is that it should be possible to make each gore from only a small number of developable elements, possibly only one, as this is the form in which the membrane material is manufactured).

We define the *equilibrium surface* of a CRTS reflector as the shape that achieves the best rms error together with an acceptable prestress distribution.

Figure 1.5 shows a small element of gore. 1 and 2 are the principal directions of curvature, and $R_1 = 1/\kappa_1$, $R_2 = 1/\kappa_2$ the corresponding principal radii. For generality, in the figure it has been assumed that the prestress distribution involves both normal stress components σ_{11} , σ_{22} , and shear stress components σ_{12} , σ_{21} . Note that $\sigma_{ii} > 0$ denotes a tensile stress. The existence of shear stress indicates that the state of prestress is not uniform.

Equilibrium in the n -direction requires (Flugge 1973, p. 20-23)

$$\frac{\sigma_{11}}{R_1} + \frac{\sigma_{22}}{R_2} = 0 \quad (1.1)$$

Depending on the shape of the gore, Eq. 1.1 will impose different conditions on the distribution of prestress, as follows.

- If $R_1 = R_2 = \infty$ (flat gore) Eq. 1.1 is satisfied by any values of σ_{11} and σ_{22} , and hence no condition is imposed.
- If $R_1 = \infty$ (cylindrical gore) Eq. 1.1 is satisfied by any value of σ_{11} , provided that

$$\sigma_{22} = 0$$

- If $R_1 > 0, R_2 > 0$ (gore of positive gaussian curvature) for any given value of σ_{11} , say, Eq. 1.1 determines σ_{22} uniquely

$$\sigma_{22} = -\frac{R_2}{R_1}\sigma_{11} \quad (1.2)$$

Since $R_2/R_1 > 0$, σ_{22} and σ_{11} have opposite signs. Hence, *a gore with positive gaussian curvature cannot be in equilibrium under a state of biaxial tension.*

- If $R_1 > 0, R_2 < 0$ —or vice-versa— (gore of negative gaussian curvature) there is again a one-to-one link between the values of σ_{11} and σ_{22} , through Eq. 1.2, but this time $R_2/R_1 < 0$ and hence both σ_{11} and σ_{22} can be positive. Hence, *a gore with negative gaussian curvature can be in equilibrium under a state of biaxial tension.*

Thus, it has been shown that the equilibrium surface of a CRTS reflector has negative gaussian curvature. It has also been shown that cylindrical gores can be subjected to uniaxial tension only, which corresponds to $\sigma_{11}/\sigma_{22} \rightarrow \infty$. Hence, a cylindrical gore can be seen as the extreme compromise between shape and prestress.

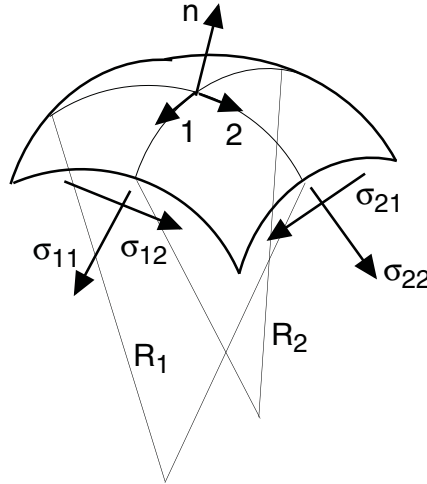


Figure 1.5: Shell element.

1.4 Design Methodology

This report investigates the possible shapes of the gores of some particular CRTS reflector configurations, both numerically and experimentally. As it is intended that the computational and experimental tools presented in this report will be used for the design of large scale CRTS reflectors, it is useful to begin with a brief review of the whole design sequence.

The following requirements are assigned at the start of the design process: aperture diameter D , focal length F , and target rms error δ . It is also assumed that the maximum permissible ratio between the highest and lowest principal stress that can be tolerated without wrinkling by the membrane material has been determined experimentally.

Given this information, the key stages of the design process are as follows.

1. Determination of the required number of ribs n , by determining the rms error of the *reference surface* of CRTS reflectors with different values of n , and with the given F and D .
2. Computation of the *equilibrium surface*, i.e. a surface whose rms error is equal to or better than δ , and such that the membrane is everywhere in biaxial tension, with an acceptable ratio between the higher and lower principal stress.
3. Computation of the cutting pattern to make a prestressed membrane whose shape approximates to the equilibrium surface, from flat membrane elements.
4. Verification that the shape and distribution of prestress in a membrane made according to (3) satisfies all the stated requirements.
5. Computation of the unstressed profile of the ribs that are required to prestress the membrane and thus achieve its predicted prestressed shape.

1.5 Layout of this Report

This report consists of two parts, one computational —Chapters 2 and 3— and one experimental —Chapters 4 and 5— followed by a discussion.

Chapter 2 presents the computational method through which the design process outlined in Section 1.4 can be executed. A series of programs, written in Matlab (Mathworks 1997) implement this design process. The theory behind these programs is presented.

Chapter 3 presents a series of predictions for CRTS reflectors of different size and with different number of ribs. Detailed predictions are presented for a reflector with $D = 1$ m and $n = 6$, a section of which has been designed and tested to validate the results from the program.

Chapter 4 describes the design of the experimental model and the material tests that were carried out. Chapter 5 describes the experiments that were carried out on the model, including the initial setup, the procedure for adjusting the pre-stress of the membrane until it becomes close to the predicted values, and the shape measurements. The results from the experiment are presented and compared to the initial predictions obtained from the program.

Chapter 6 discusses the results that have been obtained.

Chapter 2

Computational Method

2.1 Background

The determination of the equilibrium shape of a prestressed structure is called *form-finding*. In its simplest form, this problem can be dated back to Lagrange who established the equation for the equilibrium state of minimum area surfaces, Eq. 1.1. Analytical solutions of this equation are available only for simple boundary conditions (Isenberg 1992). Modern computational methods that have been developed to handle more complex shapes can be divided into two main categories, as follows.

Non-linear finite element solutions determine the large-displacement response of a membrane of pre-assigned shape, to boundary displacements and loads. An iterative solution of the membrane equations is required, due to the geometric non-linearity and the material non-linearity associated with the formation of wrinkles (see, for example, Tabarrok and Qin 1992). Outcomes of this calculation include the complete history of the prestressing process, as well as the final shape of the membrane. However, as the unstressed shape of the membrane is itself unknown in the present study, an additional level of iteration would be required.

Equilibrium methods were proposed and developed in connection with prestressed membrane roofs. The idea is to assign the state of prestress and to determine the corresponding shape of the surface required for equilibrium. Then, the prestress distribution can be adjusted in order to modify the shape of the equilibrium surface and, once this is acceptable, this abstract surface is *materialised*, i.e. the shape of the membrane from which the equilibrium surface can be realised is computed.

The two different methods that are normally used to solve the non-linear equilibrium equations associated with this method are dynamic relaxation and the force density method. In *dynamic relaxation* (Wakefield 1980; Barnes 1982; Lewis and Gosling 1993) form-finding is modelled as a pseudo-dynamic problem, where the out-of-balance forces induced by the prestress assigned in the initial configuration result in accelerations and hence motion of fictitious masses located at the nodes. Thus, the prestressed structure oscillates about its final position of equilibrium and the amplitude of this oscillation is gradually reduced by carefully selected numerical damping. It is again an iterative process, and algorithms have been suggested to accelerate the rate of convergence. A simpler and more direct method is the *force density method* (Schek 1974) where the internal force density, i.e. the ratio between the internal force and length of each element, is prescribed instead of the actual stress. The equilibrium configuration of the

prestressed structure can be found, without iteration, by solving a linear system of equations. Note, though, that whereas the prescribed force density distribution is achieved without iteration, this is not the case for the actual stress, due to length changes associated with the change from the initial to the final configuration. Typically, only a small number of iterations are required to achieve the particular stress distributions that are of interest in the present study.

2.2 Approach

Our procedure consists of four main steps. First, computation of the equilibrium surface, initially assuming that the ribs behave as rigid boundaries. In this computation the mesh of membrane elements is transformed into a virtual cable network, since the force density method cannot be applied directly to continuum elements. Thus, an equilibrium surface with the required accuracy is obtained by altering the stress within each element, by a process of trial and error. Second, the cutting pattern is computed, using a least-squares fitting of the doubly-curved equilibrium surface onto flat membrane elements. Third, an elastic analysis of this membrane is carried out, to determine its shape when it is prestressed. Finally, the unstressed profile of the ribs, which are flexible in real life, is obtained by determining the initial shape of a rib that, when subject to a distribution of forces equal and opposite to the edge reactions required for the equilibrium of the membrane, takes the shape that was initially assumed for the “rigid” boundary.

A Matlab program has been written to carry out these computations, and a series of predictions obtained from this program will be presented in this report. The program is divided into five sections.

1. Input the data file that contains the initial configuration of the mesh, i.e. node coordinates, boundary conditions, etc.
2. Computation of an acceptable equilibrium surface, by trial and error.
3. Computation of cutting pattern, i.e. the profile of a flat membrane with curved edges to form approximately the required doubly-curved shape.
4. Elastic analysis of the membrane defined in (3), to ensure that its shape satisfies the accuracy requirement.
5. Beam analysis, to calculate the required rib profile.

2.3 Mesh and Boundary Conditions

The initial input shape for our antenna reflector is a paraboloid of revolution, described by the function

$$Z = (X^2 + Y^2)/4F \quad (2.1)$$

where F is the focal length, and the Z -axis is an axis of rotational symmetry. In a symmetric CRTS reflector with n ribs it is sufficient to analyse a sector bounded by

two adjacent ribs. In fact, the size of the computation could be further reduced by considering only half of a sector, but this will not be done here, because it is intended to extend the present analysis to offset reflectors.

Two types of elements are defined, the membrane elements representing the surface and the cable elements representing the cable along the top edge of the membrane. A typical mesh is shown in Fig. 2.1 in plan view. The membrane mesh is defined by two numbers, i.e. the sub-divisions along the hub attachment and along the rib; in Fig. 2.1 these numbers are respectively 4 and 12. The X, Y coordinates of each node are defined such that the projection of the mesh onto the $X-Y$ plane is a uniform grid; the Z -coordinate is calculated from Eq. 2.1. The numbering of the nodes goes from the bottom left to the top right corner. Along the top edge of the membrane a series of cable elements are defined, forming a tensioned edge for the gore.

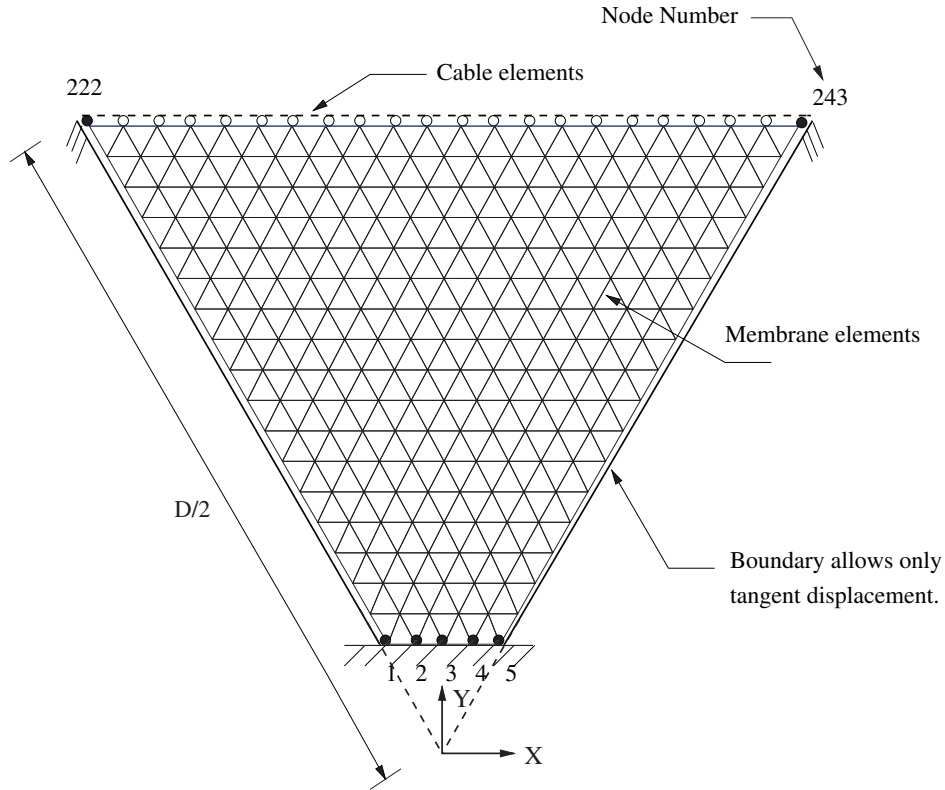


Figure 2.1: Initial mesh, plan view.

The following boundary conditions are applied. The bottom nodes of the membrane, i.e. nodes 1 to 5 in Fig. 2.1, connect the membrane to the rigid hub, and hence are fully constrained. The tip nodes, 222 and 243, are also fully constrained, as the membrane is fully connected to the ribs at these points. All other nodes on the side edges are free to slide in a direction tangent to the parabola defined by the intersection of Eq. 2.1 with the two radial planes that bound the sector, but are otherwise constrained. This is equivalent to saying that the membrane can slide over the two edge ribs, which have been assumed to be infinitely rigid. All other nodes are unconstrained.

2.4 Computation of Equilibrium Surface

The force density method, originally developed for cable network structures (Schek 1974), is used to calculate the shape of the equilibrium surface. Consider node i of the cable network shown in Fig. 2.2a. It is connected to nodes j, k , etc. by cables of lengths L_{ij} , L_{ik} , etc and is subjected to an external force p_i . Denoting by F_{ij} , etc. the axial forces in the cable elements, the equilibrium equations for node i can be written in terms of the nodal coordinates X_i, Y_i, Z_i , etc. as follows

$$\begin{aligned} F_{ij} \frac{X_j - X_i}{L_{ij}} + F_{ik} \frac{X_k - X_i}{L_{ik}} + \dots &= p_{iX} \\ F_{ij} \frac{Y_j - Y_i}{L_{ij}} + F_{ik} \frac{Y_k - Y_i}{L_{ik}} + \dots &= p_{iY} \\ F_{ij} \frac{Z_j - Z_i}{L_{ij}} + F_{ik} \frac{Z_k - Z_i}{L_{ik}} + \dots &= p_{iZ} \end{aligned} \quad (2.2)$$

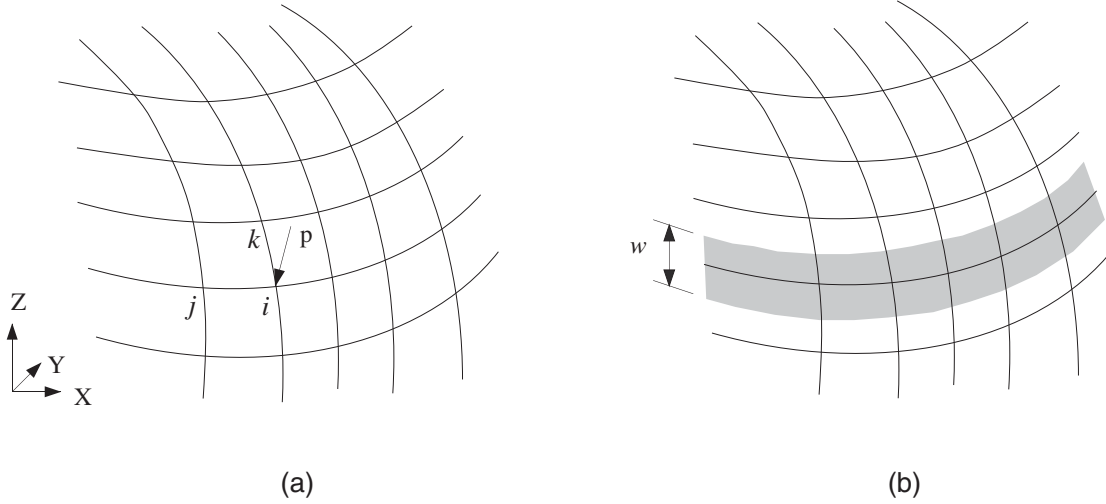


Figure 2.2: (a) Cable network and (b) network equivalent to a given membrane surface.

Introducing for each cable element a *force density*, i.e. the ratio between the force in the cable and its length, we have

$$f_{ij} = \frac{F_{ij}}{L_{ij}}, \text{ etc.} \quad (2.3)$$

In this method the force density in each cable of the network is assigned at the beginning of the form-finding computation. Then, Eq. 2.2 can be re-written as:

$$\begin{aligned}
f_{ij}(X_j - X_i) + f_{ik}(X_k - X_i) + \dots &= p_{iX} \\
f_{ij}(Y_j - Y_i) + f_{ik}(Y_k - Y_i) + \dots &= p_{iY} \\
f_{ij}(Z_j - Z_i) + f_{ik}(Z_k - Z_i) + \dots &= p_{iZ}
\end{aligned} \tag{2.4}$$

Similar equilibrium equations can be written for all unconstrained nodes of the cable network, whereas a reduced set of equations is written at partially constrained nodes. A system of linear equations is thus obtained, and the nodal coordinates can be obtained by solving this system.

Then, the length of each cable element can be computed from the nodal coordinates, and hence the actual force in the element is

$$F_{ij} = f_{ij} \sqrt{(X_j - X_i)^2 + (Y_j - Y_i)^2 + (Z_j - Z_i)^2} \tag{2.5}$$

This technique is very efficient because there is no iteration involved and it can be extended to membrane structures with some simple modifications.

Some types of membranes consist of two-way fibres, woven together without any additional binding material. In such membranes the deformation in one fibre direction does not affect the other direction, and there is no shear stress hence a width w of membrane can be modelled as a cable, see Fig. 2.2b (Grundig and Moncrieff 1993). The force density method is directly applicable to membranes of this type. The membrane is divided into a grid of virtual cable elements, and each cable force is given by the product of stress by thickness by width of membrane, see the shaded area in Fig. 2.2b.

This approach, though, is not valid for CRTS reflectors because the membrane material, Kapton or Kevlar-reinforced Kapton foil, is able to carry shear stress. In this case, the membrane needs to be simulated by a different kind of virtual cable network, which allows for biaxial stress coupling. This is achieved by means of a triangulated grid.

A link will now be established between the stresses in the membrane and the cable forces in a virtual triangulated network, using a finite element formulation. In the standard formulation of the constant strain triangular element (Cook et al. 1989), shown in Fig. 2.3a, the following relationship is established between the nodal forces and the stress components

$$\mathbf{p} = \Delta h \mathbf{B}^T \mathbf{s} \tag{2.6}$$

where

$$\begin{aligned}
\Delta &= \text{element area} \\
h &= \text{element thickness} \\
\mathbf{p} &= [p_{1x} \ p_{1y} \ p_{2x} \ p_{2y} \ p_{3x} \ p_{3y}]^T \\
\mathbf{s} &= [\sigma_{xx} \ \sigma_{yy} \ \tau_{xy}]^T \\
\mathbf{B} &= \frac{1}{2\Delta} \begin{bmatrix} b_1 & 0 & b_2 & 0 & b_3 & 0 \\ 0 & c_1 & 0 & c_2 & 0 & c_3 \\ c_1 & b_1 & c_2 & b_2 & c_3 & b_3 \end{bmatrix}
\end{aligned}$$

and

$$\begin{aligned} b_1 &= y_2 - y_3, & b_2 &= y_3 - y_1, & b_3 &= y_1 - y_2, \\ c_1 &= x_3 - x_2, & c_2 &= x_1 - x_3, & c_3 &= x_2 - x_1. \end{aligned}$$

Note the use of a local coordinate system, where x, y are coplanar with the element.

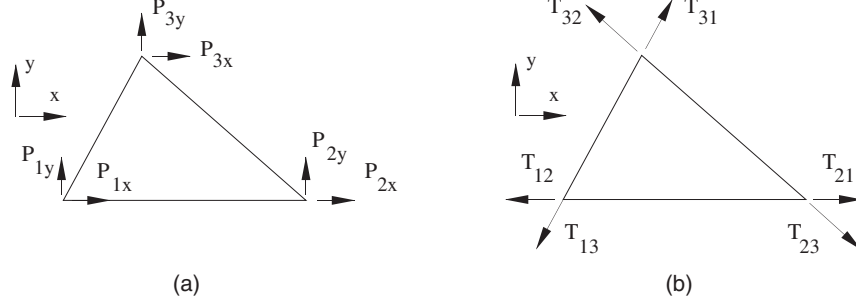


Figure 2.3: (a) Standard, constant stress triangular element; (b) same element with nodal force components in the directions of the edges.

Next, following an approach in Przemieniecki (1968), the cartesian nodal force components are transformed into a skew system parallel to the edges of the element, as shown in Fig. 2.3b. For example, considering node 1,

$$\begin{bmatrix} p_{1x} \\ p_{1y} \end{bmatrix} = \begin{bmatrix} -c_3/L_{12} & c_2/L_{13} \\ b_3/L_{12} & -b_2/L_{13} \end{bmatrix} \begin{bmatrix} T_{12} \\ T_{13} \end{bmatrix} \quad (2.7)$$

Defining

$$\begin{aligned} t_{12} &= T_{12}/L_{12} \\ t_{13} &= T_{13}/L_{13} \end{aligned} \quad (2.8)$$

Note that Eq. 2.8

$$\begin{bmatrix} p_{1x} \\ p_{1y} \end{bmatrix} = \begin{bmatrix} -c_3 & c_2 \\ b_3 & -b_2 \end{bmatrix} \begin{bmatrix} t_{12} \\ t_{13} \end{bmatrix} \quad (2.9)$$

Inverting this equation gives

$$\begin{bmatrix} t_{12} \\ t_{13} \end{bmatrix} = \frac{1}{c_2 b_3 - c_3 b_2} \begin{bmatrix} b_2 & c_2 \\ b_3 & c_3 \end{bmatrix} \begin{bmatrix} p_{1x} \\ p_{1y} \end{bmatrix} \quad (2.10)$$

Proceeding in the same way for the other two nodes of the element, and noting that

$$-2\Delta = c_2 b_3 - c_3 b_2 = c_3 b_1 - c_1 b_3 = c_1 b_2 - c_2 b_1 \quad (2.11)$$

the following transformation equation is obtained

$$\begin{bmatrix} t_{12} \\ t_{13} \\ t_{21} \\ t_{23} \\ t_{31} \\ t_{32} \end{bmatrix} = -\frac{1}{2\Delta} \begin{bmatrix} b_2 & c_2 & 0 & 0 & 0 & 0 \\ b_3 & c_3 & 0 & 0 & 0 & 0 \\ 0 & 0 & b_1 & c_1 & 0 & 0 \\ 0 & 0 & b_3 & c_3 & 0 & 0 \\ 0 & 0 & 0 & 0 & b_1 & c_1 \\ 0 & 0 & 0 & 0 & b_2 & c_2 \end{bmatrix} \mathbf{p} \quad (2.12)$$

Substituting Eq. 2.6 for \mathbf{p} , simplifying and carrying out the required matrix multiplication gives

$$\begin{bmatrix} t_{12} \\ t_{13} \\ t_{21} \\ t_{23} \\ t_{31} \\ t_{32} \end{bmatrix} = -\frac{h}{4\Delta} \begin{bmatrix} b_1 b_2 & c_1 c_2 & b_1 c_2 + b_2 c_1 \\ b_3 b_1 & c_3 c_1 & b_3 c_1 + b_1 c_3 \\ b_1 b_2 & c_1 c_2 & b_1 c_2 + b_2 c_1 \\ b_2 b_3 & c_2 c_3 & b_2 c_3 + b_3 c_2 \\ b_3 b_1 & c_3 c_1 & b_3 c_1 + b_1 c_3 \\ b_2 b_3 & c_2 c_3 & b_2 c_3 + b_3 c_2 \end{bmatrix} \begin{bmatrix} \sigma_{xx} \\ \sigma_{yy} \\ \tau_{xy} \end{bmatrix} \quad (2.13)$$

However, noting that $t_{ij} = t_{ji}$, only three of the above equations are independent, which leaves

$$\begin{bmatrix} t_{12} \\ t_{23} \\ t_{31} \end{bmatrix} = -\frac{h}{4\Delta} \begin{bmatrix} b_1 b_2 & c_1 c_2 & b_1 c_2 + b_2 c_1 \\ b_2 b_3 & c_2 c_3 & b_2 c_3 + b_3 c_2 \\ b_3 b_1 & c_3 c_1 & b_3 c_1 + b_1 c_3 \end{bmatrix} \begin{bmatrix} \sigma_{xx} \\ \sigma_{yy} \\ \tau_{xy} \end{bmatrix} \quad (2.14)$$

Defining

$$\mathbf{t} = [t_{12} \quad t_{23} \quad t_{31}]^T$$

Equation 2.14 becomes

$$\mathbf{t} = -\frac{h}{4\Delta} \begin{bmatrix} b_1 b_2 & c_1 c_2 & b_1 c_2 + b_2 c_1 \\ b_2 b_3 & c_2 c_3 & b_2 c_3 + b_3 c_2 \\ b_3 b_1 & c_3 c_1 & b_3 c_1 + b_1 c_3 \end{bmatrix} \mathbf{s} \quad (2.15)$$

Note that \mathbf{t}/h can be interpreted as the three shear stresses along the sides of the triangular element.

Equation 2.14 defines the three force densities for a constant stress triangular element. For a given stress distribution over a membrane that has been divided up into small triangles, Eq. 2.14 can be used to calculate—for each triangle—the three force densities for the virtual cable network. Note that, as each triangular element is replaced by three cables, this procedure yields two overlapping cables along the common interface between two triangles.

The shape of this virtual cable network can then be determined by solving a system of linear equilibrium equations analogous to Eq. 2.4. No iteration is required to solve this system but, unlike the solution obtained for a real cable net, this time the solution is approximate. This is because the area, Δ , of the triangular elements, used in Eq. 2.14 for the conversion of stress into force densities, cannot be calculated exactly before knowing the final shape. Therefore, an iterative refinement of the solution is required.

2.4.1 Procedure

The procedure for determining the equilibrium surface for a gore of the CRTS reflector is, therefore, as follows.

1. Divide the gore into a set of small triangular elements;
2. Assume a stress distribution, i.e. prescribe the values of the stress components in local coordinates σ_{xx} , σ_{yy} and τ_{xy} in each triangle;
3. Replace each triangle with three cables and compute the force densities in these cables using Eq. 2.14;
4. Assemble the equilibrium equations for the virtual cable net;
5. Solve the equilibrium equations to find the nodal coordinates;
6. Calculate the stress components in each membrane element, using the newly obtained nodal coordinates, by solving Eq. 2.14 with the updated value of Δ .

Check the accuracy of the solution. If it is not satisfied, return to step (3) and repeat;

7. Determine the rms error of the current equilibrium surface, see Appendix A.

If the rms error is not acceptable, modify the stress distribution in step (2) and repeat.

8. Check that in all elements the current principal stresses are both positive, or greater than a specified minimum value.

2.5 Computation of Cutting Pattern

In the case of a cable network, the determination of the “cutting pattern”, i.e. of the unstressed lengths of the cable segments, is straightforward, and the prestressed equilibrium shape can be practically realised without introducing any approximations. If a cable segment has a stressed length of L when it is subject to the stress σ , its unstressed length L_0 is

$$L_0 = \frac{L}{1 + \sigma/E} \quad (2.16)$$

In the case of a doubly-curved equilibrium surface, determining the cutting pattern consists in computing the edge of the pieces of flat membrane from which the surface can be formed. When these pieces are joined together along their edges and are prestressed, the shape of the membrane needs to approximate closely to the equilibrium surface. The cutting pattern is computed in two separate steps. First, *elastic de-stressing* of the equilibrium surface, using a finite element analysis and, second, *geometric projection* using least-squares.

The de-stressing step is required because the equilibrium surface is a prestressed shape, whereas the cutting operation can only be carried out on an unstressed membrane. The de-stressing is done by reversing the stress distribution of the prestressed membrane. The nodal forces induced by the reversed stresses are computed using Eq. 2.6 and the corresponding nodal displacements are determined by a standard, linear-elastic finite element analysis. The stiffness matrix for each element is

$$\mathbf{K} = \Delta h \mathbf{B}^T \mathbf{D} \mathbf{B} \quad (2.17)$$

where, assuming the membrane to be *isotropic* the material elasticity matrix has the expression

$$\mathbf{D} = \frac{E}{1 - \nu^2} \begin{bmatrix} 1 & \nu & 0 \\ \nu & 1 & 0 \\ 0 & 0 & \frac{1-\nu}{2} \end{bmatrix} \quad (2.18)$$

The fixed boundaries are removed during this process, and hence the structure that is being analysed is capable of rigid-body motions.

The shape obtained thus is usually doubly-curved, and hence not developable, and needs to be projected onto a flat surface to determine the cutting pattern. The error associated with this projection can be reduced by dividing the doubly-curved shape into two or more parts before projecting each one of them. The most commonly used and simplest method for doing this is known as *elemental unfolding* (Grundig and Bahndorf 1988). The idea is to determine by finite-element analysis the stress distribution required to flatten each part of the membrane. If the required stresses are too large, the membrane is divided into smaller parts and the stress distribution in each part is computed. This method is good mainly for applications where the stress distribution is more important than the surface shape that is obtained. A comparison of various available techniques has been recently published (Galasko et al. 1997).

To achieve high geometrical precision, a least squares projection will be adopted. The projection method is based on the principle that the distance between any two points on a curved surface should be as close as possible to the distance of the same two points after projection onto a plane. Ideally, the distance between the two points on the curved surface should be measured along a geodetic line but, because the elements used in the shape finding analysis are very small, it is accurate enough to take the arc-length to be approximately equal to the length of a straight segment between the two points. Thus, the distance between the two points can be calculated, see Fig. 2.4, from

$$\sqrt{(\bar{x}_1 - \bar{x}_2)^2 + (\bar{y}_1 - \bar{y}_2)^2} = \sqrt{(X_1 - X_2)^2 + (Y_1 - Y_2)^2 + (Z_1 - Z_2)^2} \quad (2.19)$$

which is equivalent to

$$(\bar{x}_1 - \bar{x}_2)^2 + (\bar{y}_1 - \bar{y}_2)^2 = (X_1 - X_2)^2 + (Y_1 - Y_2)^2 + (Z_1 - Z_2)^2 \quad (2.20)$$

Here, \bar{x}_1 , \bar{y}_1 , \bar{x}_2 and \bar{y}_2 are unknowns but, assuming that the X, Y nodal coordinates of any node do not change by very much during the projection, we write

$$\bar{x}_1 = X_1 + d\bar{x}_1, \quad \bar{y}_1 = Y_1 + d\bar{y}_1, \quad \text{etc.} \quad (2.21)$$

where $d\bar{x}_1, d\bar{y}_1$ etc. are small in comparison with X_1, Y_1 etc. Substituting Eq. 2.21 into Eq. 2.20 and re-arranging yields

$$\begin{aligned} (X_1 - X_2)^2 + 2(X_1 - X_2)(d\bar{x}_1 - d\bar{x}_2) + (d\bar{x}_1 - d\bar{x}_2)^2 + \dots \\ = (X_1 - X_2)^2 + (Y_1 - Y_2)^2 + (Z_1 - Z_2)^2 \end{aligned} \quad (2.22)$$

Simplifying and neglecting higher-order terms

$$2(X_1 - X_2)(d\bar{x}_1 - d\bar{x}_2) + 2(Y_1 - Y_2)(d\bar{y}_1 - d\bar{y}_2) = (Z_1 - Z_2)^2 \quad (2.23)$$

This is a linear equation in $d\bar{x}_1, d\bar{y}_1$, etc. An equation of this type can be written for each side of a triangular element, but it is written only once for a side that is common to two elements. Consider, for example, the simple gore discretisation shown in Fig. 2.4. By applying Eq. 2.23 to each triangle side, we obtain a system of 38 equations in $18 \times 2 - 3 = 33$ unknowns. This is an over-determinate system which is solved by least-squares. The three unknowns that have been subtracted from this count correspond to the three rigid-body motions of the whole cutting pattern, in the plane. One may assume, for example, $d\bar{x}_1 = d\bar{y}_1 = d\bar{y}_2 = 0$.

In general, this solution will be asymmetric, which may be undesirable. In the case of symmetric reflectors, this asymmetry can be eliminated by averaging the values on either side of the centre line of each gore. If a non-symmetric cutting pattern is being produced, it is important to ensure that the boundary lengths of adjacent gores maintain exactly their correct length, to avoid any mismatch when these adjacent gores are bonded together. Therefore, a weighting factor is introduced into the least squares projection, to increase the accuracy of the boundary lengths.

2.6 Elastic Analysis

An elastic analysis is carried out to determine the prestressed shape of a reflector made from the flat gores computed in Section 2.5. The most efficient way of doing this is to take the equilibrium surface as a reference, and to formulate the elastic analysis in terms of a small variation from this shape. This has the advantage that the displacements that have to be computed are quite small, and hence only one or two iterations are required. However, the approach required is quite subtle, and needs to be explained carefully.

We begin by considering what would happen to a general triangular element 123 that forms the equilibrium surface computed in Section 2.4 if it was made of elastic material, and prestressed exactly in the way that we have computed, in the position that we have computed. Let Fig. 2.5a be a schematic view of this elastic element. Note that, since the element is being considered on its own, for it to be in equilibrium under the required prestress \mathbf{s} , nodal forces p_{1x}, p_{1y} , etc. have to be applied at the corners.

Next, consider the element 123 after de-stressing. It will be a little bit smaller, as shown in Fig. 2.5b, and the nodal forces will be zero. The elastic deformation that occurs

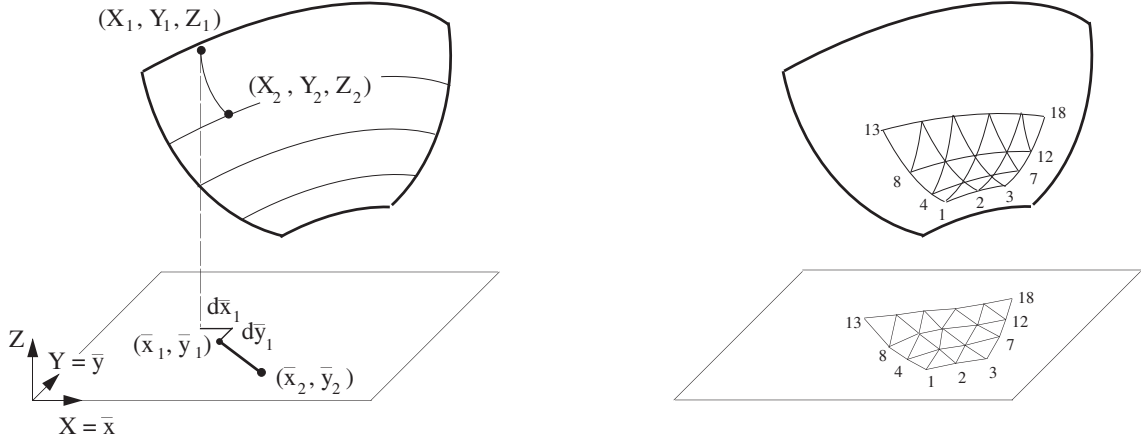


Figure 2.4: Surface projection.

in going from configuration (a) to (b) is the effect of applying the loads $-p_{1x}$, $-p_{1y}$, etc. to the element. Finally, consider the same element after the *whole mesh* has been projected onto a flat gore, Fig. 2.5c. Note that the element is no longer unstressed, as the approximations involved in the cutting pattern calculation amount to applying a certain level of strain to the element. Let ds be the current stress. Also note that, for the element to be in equilibrium, nodal forces dp_{1x} , dp_{1y} , etc. have to be applied.

Since the nodal coordinates in configurations (a) and (c) are known, we can compute the side lengths of the element from

$$\begin{aligned} \text{e.g. } L_{12} &= \sqrt{(X_2 - X_1)^2 + (Y_2 - Y_1)^2 + (Z_2 - Z_1)^2}, \\ l_{12} &= \sqrt{(\bar{x}_2 - \bar{x}_1)^2 + (\bar{y}_2 - \bar{y}_1)^2}, \text{ etc.} \end{aligned}$$

and hence the linear strains along the direction of the sides are

$$\epsilon_{12} = \frac{l_{12} - L_{12}}{L_{12}}, \quad \text{etc.} \quad (2.24)$$

To convert these linear strains into ϵ_{xx} , ϵ_{yy} , γ_{xy} we will use the standard strain transformation (Gere and Timoshenko 1990). Hence, we need to determine the direction cosines of sides 23 and 13 with respect to the x, y coordinate system (note that side 12 coincides with the x -axis). We can do this either for configuration (a) or (c): since the strains involved are small, either configuration is acceptable and we will choose (c) for simplicity.

Define unit vectors \mathbf{i}, \mathbf{j} , parallel to x, y , and $\mathbf{u}_1, \mathbf{u}_2$ parallel to 12, 23, as follows

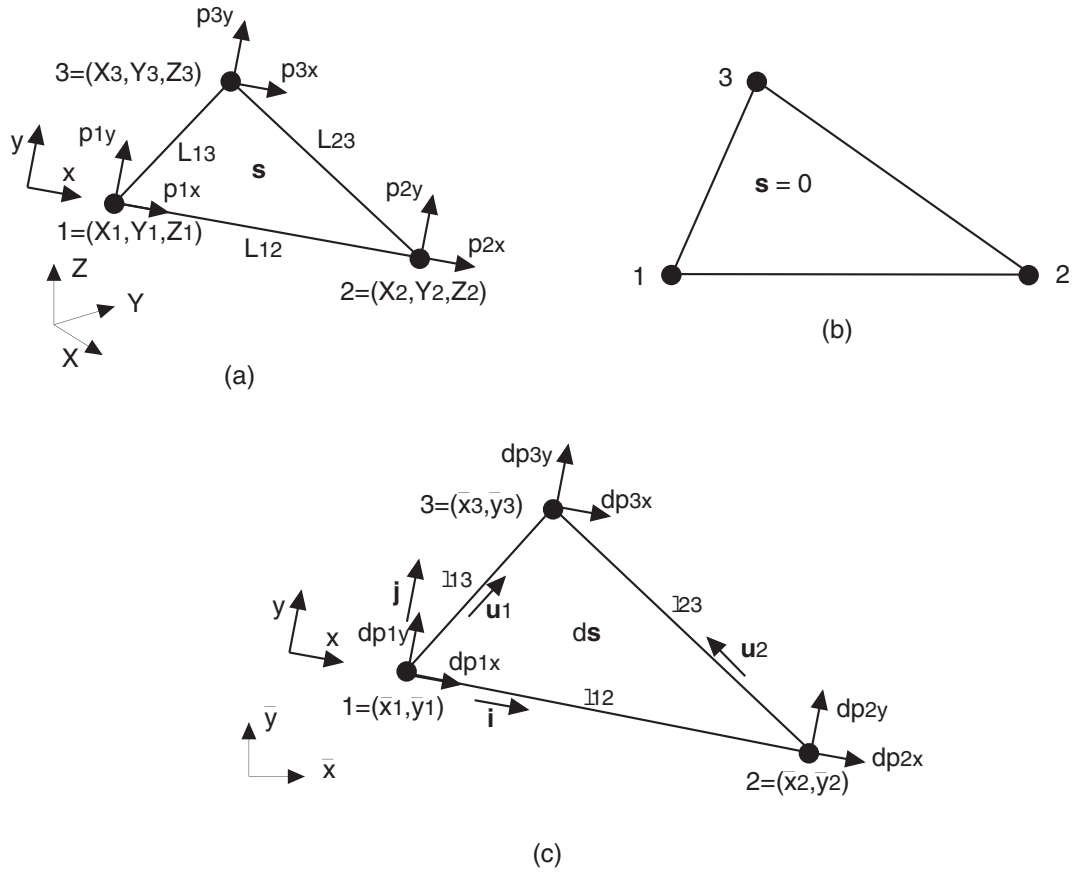


Figure 2.5: Configurations of an elastic membrane element; (a) within the equilibrium surface; (b) de-stressed; (c) within the cutting pattern.

$$\mathbf{i} = \frac{\begin{bmatrix} \bar{x}_2 - \bar{x}_1 & \bar{y}_2 - \bar{y}_1 \end{bmatrix}^T}{\sqrt{(\bar{x}_2 - \bar{x}_1)^2 + (\bar{y}_2 - \bar{y}_1)^2}} \quad (2.25)$$

$$\mathbf{j} = \frac{\begin{bmatrix} \bar{y}_1 - \bar{y}_2 & \bar{x}_2 - \bar{x}_1 \end{bmatrix}^T}{\sqrt{(\bar{x}_2 - \bar{x}_1)^2 + (\bar{y}_2 - \bar{y}_1)^2}} \quad (2.26)$$

$$\mathbf{u}_1 = \frac{\begin{bmatrix} \bar{x}_3 - \bar{x}_1 & \bar{y}_3 - \bar{y}_1 \end{bmatrix}^T}{\sqrt{(\bar{x}_3 - \bar{x}_1)^2 + (\bar{y}_3 - \bar{y}_1)^2}} \quad (2.27)$$

$$\mathbf{u}_2 = \frac{\begin{bmatrix} \bar{x}_3 - \bar{x}_2 & \bar{y}_3 - \bar{y}_2 \end{bmatrix}^T}{\sqrt{(\bar{x}_3 - \bar{x}_2)^2 + (\bar{y}_3 - \bar{y}_2)^2}} \quad (2.28)$$

The relationship between $\epsilon_{xx}, \epsilon_{yy}, \gamma_{xy}$ and $\epsilon_{12}, \epsilon_{13}, \epsilon_{23}$ is given by

$$\begin{bmatrix} 1 & 0 & 0 \\ (\mathbf{u}_2 \cdot \mathbf{i})^2 & (\mathbf{u}_2 \cdot \mathbf{j})^2 & (\mathbf{u}_2 \cdot \mathbf{i})(\mathbf{u}_2 \cdot \mathbf{j}) \\ (\mathbf{u}_1 \cdot \mathbf{i})^2 & (\mathbf{u}_1 \cdot \mathbf{j})^2 & (\mathbf{u}_1 \cdot \mathbf{i})(\mathbf{u}_1 \cdot \mathbf{j}) \end{bmatrix} \begin{bmatrix} \epsilon_{xx} \\ \epsilon_{yy} \\ \gamma_{xy} \end{bmatrix} = \begin{bmatrix} \epsilon_{12} \\ \epsilon_{23} \\ \epsilon_{13} \end{bmatrix} \quad (2.29)$$

An equivalent relationship was derived by Lewis and Gosling (1993). Equation 2.29 can be solved for

$$\mathbf{e} + d\mathbf{e} = \begin{bmatrix} \epsilon_{xx} & \epsilon_{yy} & \gamma_{xy} \end{bmatrix}^T \quad (2.30)$$

The corresponding stress components are

$$\mathbf{s} + d\mathbf{s} = \mathbf{D}(\mathbf{e} + d\mathbf{e}) \quad (2.31)$$

and, substituting $\mathbf{s} + d\mathbf{s}$ into Eq. 2.6

$$\mathbf{p} + d\mathbf{p} = \Delta h \mathbf{B} \mathbf{D}(\mathbf{e} + d\mathbf{e}) \quad (2.32)$$

In the elastic analysis only the nodal forces $d\mathbf{p}$ will be considered, because it is already known from Section 2.4 that \mathbf{p} is in equilibrium with the prestress \mathbf{s} . Therefore, instead of using Eq. 2.32 we compute

$$d\mathbf{p} = (\mathbf{p} + d\mathbf{p}) - \mathbf{p} = \Delta h \mathbf{B} [\mathbf{D}(\mathbf{e} + d\mathbf{e}) - \mathbf{s}] \quad (2.33)$$

After computing the nodal forces $d\mathbf{p}$ for each element, we set up the stiffness matrix for the complete mesh of triangular elements in configuration (a), i.e. the equilibrium configuration, and apply the nodal forces $d\mathbf{p}$ onto it, in order to determine the deviations from the equilibrium configuration. It has been found that often $d\mathbf{p}$ is sufficiently small that this calculation can be done in a single step.

Note that the stiffness matrix that is considered at this stage consists of Eq. 2.17 plus the geometric stiffness matrix, which accounts for the geometric stiffness resulting from the stress \mathbf{s} .

2.7 Rib Profile

In the foregoing analysis the ribs have been modelled as a rigid boundary but, in practice, they are realised by means of thin-walled, flexible elements. Their shape changes under the forces applied by the membrane need to be taken into account when determining the shape in which they should be manufactured. Due to symmetry, this shape is the same for all ribs.

A rib is modelled as a cantilever, Fig. 2.6, consisting of beam elements linking the edge nodes of the membrane. The coordinates of these nodes are the same that were computed in Section 2.6, and the nodal load components are the edge reactions on the membrane, also computed in Section 2.6.

Note that these applied forces are opposite to those applied by the membrane to the rib. Due to these forces, the rib deflects back to the initial profile in which it should be made. When a rib of this shape is subject to the membrane edge forces, it will take the shape of the “rigid” boundary that was assumed throughout the shape and stress analysis.

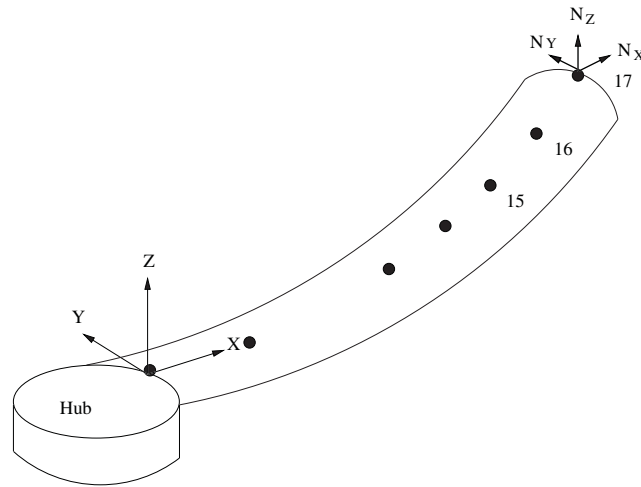


Figure 2.6: Force components on a rib.

Chapter 3

Computational Results

3.1 Introduction

This chapter makes use of the Matlab programs that implement the procedure developed in Chapter 2 to carry out the following.

- A detailed design of a 1 m diameter symmetric reflector with 6 ribs, a physical model of which will be used to verify the computational analysis, in Chapter 4.
- A series of computations of the rms error of reflectors of different apertures ($D = 1$ - 10 m) and different numbers of ribs ($n = 6$ - 24), but with the same $F/D = 0.78$.

3.2 Analysis of 1 m Reflector with 6 Ribs

A symmetric reflector with $D = 1$ m aperture and $n = 6$ ribs was chosen to carry out a comparison between the computational method developed in Chapter 2 and experimental measurements. These particular values of D and n were chosen to minimise gravity effects, hence D had to be small, while avoiding membrane gores that are too narrow, and hence more sensitive to errors in the cutting pattern.

Following Eq. 2.1, the target shape of the reflector model was chosen to be

$$Z = \frac{X^2 + Y^2}{4 \times 0.78} = 0.32(X^2 + Y^2) \quad (3.1)$$

which gives $Z_{max} \approx 0.08$ m at the edge, i.e. for $\sqrt{X^2 + Y^2} = 0.5$ m. The focal distance of a reflector with this shape is 0.78 m, and hence $F/D = 0.78$.

Figure 3.1 shows the initial mesh, both in side and plan views, consisting of 243 nodes, 425 membrane elements, and 21 cable elements. The initial coordinates of the nodes were defined as explained in Section 2.3.

3.2.1 Equilibrium surface

The computation of the equilibrium surface was started by assigning a uniform prestress distribution in all elements, as follows

$$\mathbf{s}h = h [\sigma_{xx} \quad \sigma_{yy} \quad \tau_{xy}]^T = [170 \quad 170 \quad 0]^T \quad \text{N/m}$$

Note that these stress components are defined in the local coordinate system for each triangular element, where the x -axis is parallel to the X -axis, and the y -axis is parallel to the YZ plane. The cable force along the outer edge of the gore was assumed to be 90 N.

Figure 3.2 shows the equilibrium surface obtained after completing the computation described in Section 2.4.1. After about twenty trial-and-error iterations the selected shape had an rms error of 3.5 mm. The side view of this equilibrium surface shows that the membrane is doubly curved to a small extent. The transverse curvature could be reduced, thus approaching the reference surface whose rms error is 3.0 mm, by increasing the transverse stress, but this would be at the expense of a less desirable stress distribution.

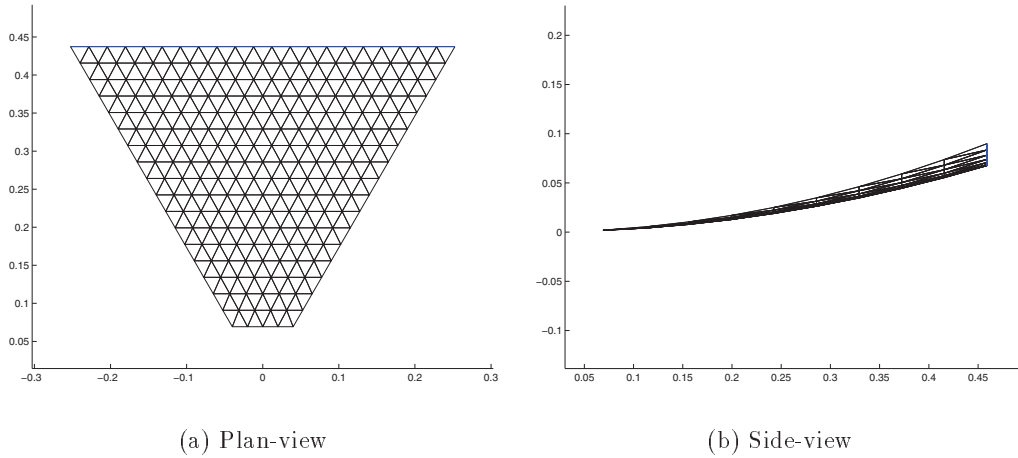
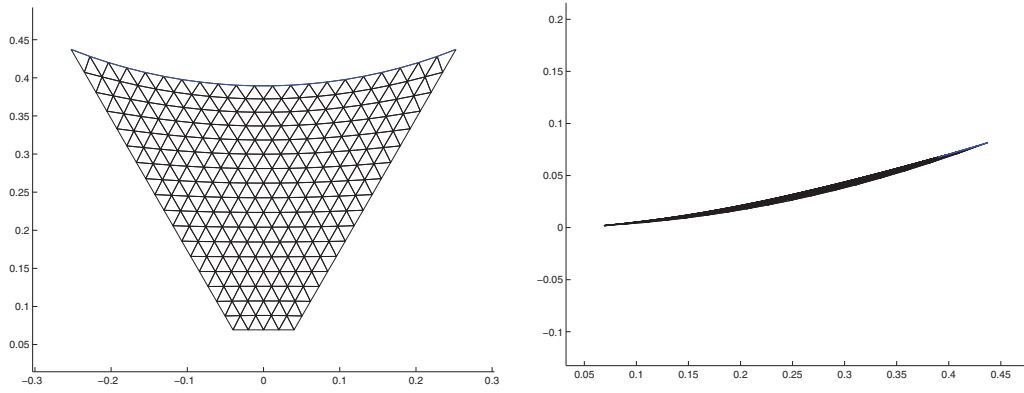


Figure 3.1: Initial mesh.

The stress distribution that corresponds to the equilibrium surface is shown in Fig. 3.3 in terms of the x, y stress components. Note that the stress distribution appears fairly uniform, i.e. the ratio $\sigma_{xx} / \sigma_{yy}$ is close to 1, although significantly different from the initially assumed magnitude of 170 N/m. This plot will be useful when planning the location for the strain gauges that will be used to measure the stress field, as the direction of these gauges is roughly the same as the local element axes.

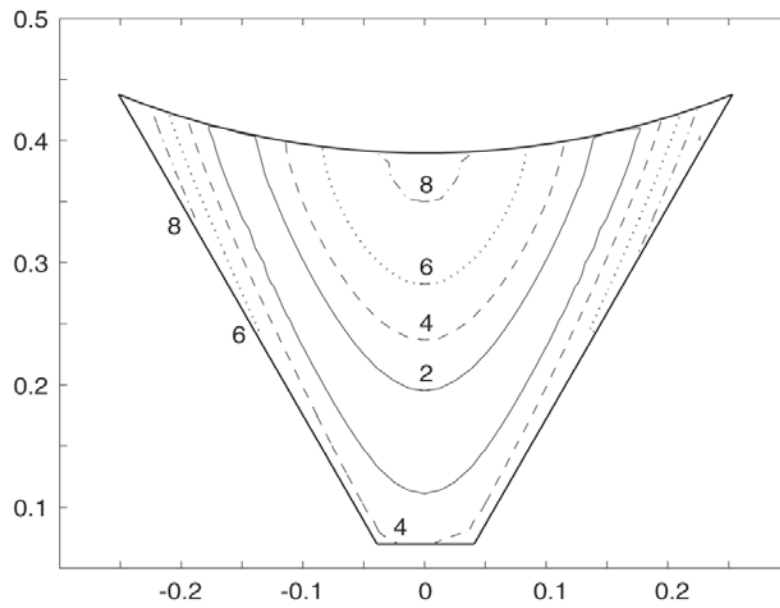
The stress field is also shown in Fig. 3.4, in terms of principal stress components, where $\sigma_{11} \geq \sigma_{22}$. The three plots in Fig. 3.4 show that the highest value of $\sigma_{11}h$ is 293 N/m, at the top corners of the membrane. Here, $\sigma_{22}h$ is at its lowest, 100 N/mm, and hence the maximum stress ratio is 3. The highest value of $\sigma_{22}h$ is 169 N/m at the centre of the membrane. Here, the stress ratio is about one.

Achieving an even, biaxial stress distribution is desirable to avoid wrinkling, and Fig. 3.4 shows that the stress distribution in the equilibrium surface satisfies the condition $\sigma_{11}/\sigma_{22} < 1.8$ almost everywhere.



(a) Top-view

(b) Side-view



(c) Error with respect to best fit paraboloid [mm].

Figure 3.2: Equilibrium surface.

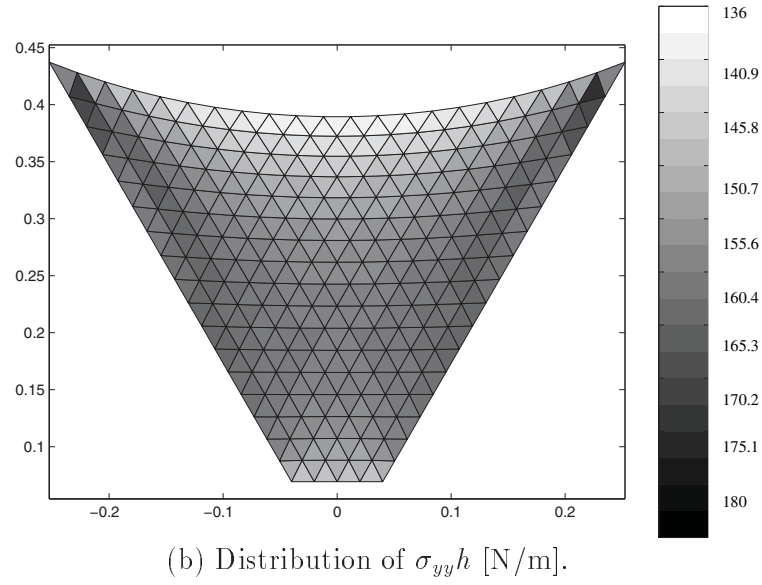
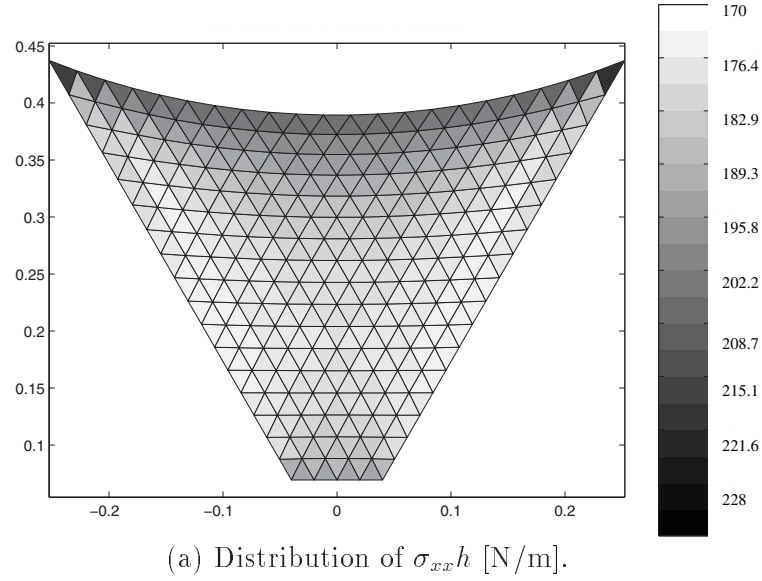
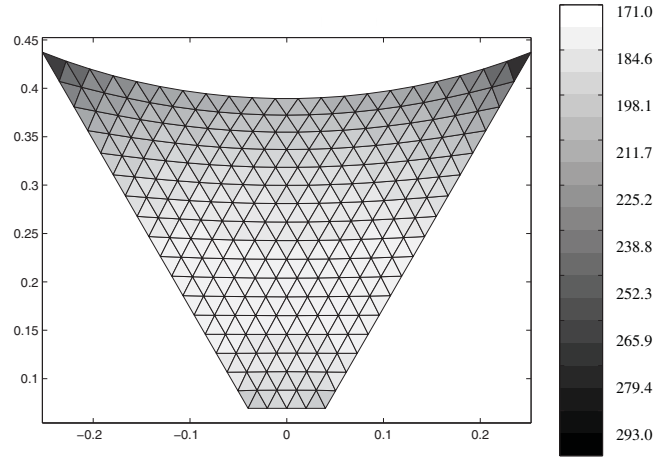
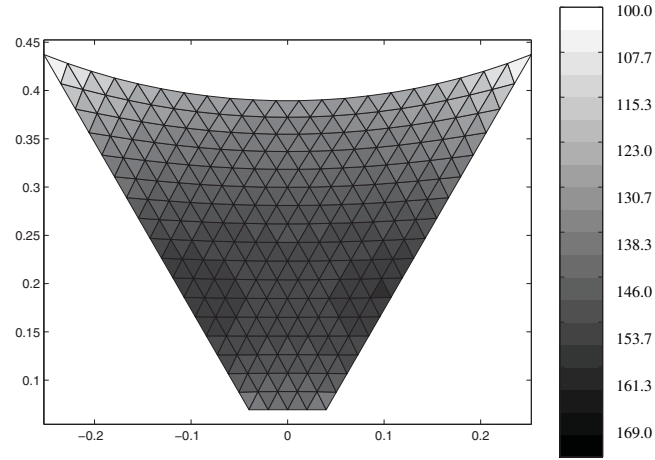


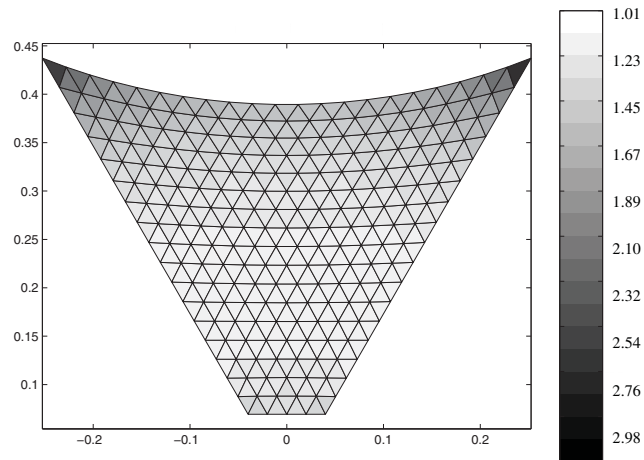
Figure 3.3: Equilibrium surface, predicted stress distribution.



(a) Principal stress $\sigma_{11} h$ [N/m].



(b) Principal stress $\sigma_{22} h$ [N/m].



(c) Ratio σ_{11}/σ_{22} .

Figure 3.4: Equilibrium surface, predicted stress distribution.

A different type of plot of the stress distribution is shown in Fig. 3.5. This plot shows both the direction and magnitude of the principal stresses, and thus makes it possible to identify the stress trajectories in the membrane. The plot shows that the principal stress directions vary along the surface and, close to the side edges, rotate by as much as 45° . Depending on what type of membrane is chosen for the CRTS reflector, whether fibre-reinforced or not, this results indicates that if the fibre directions do not coincide with the principal stress directions, the elasticity matrix for an isotropic material used in Eq. 2.18 might have to be replaced with the appropriate orthotropic elasticity matrix.

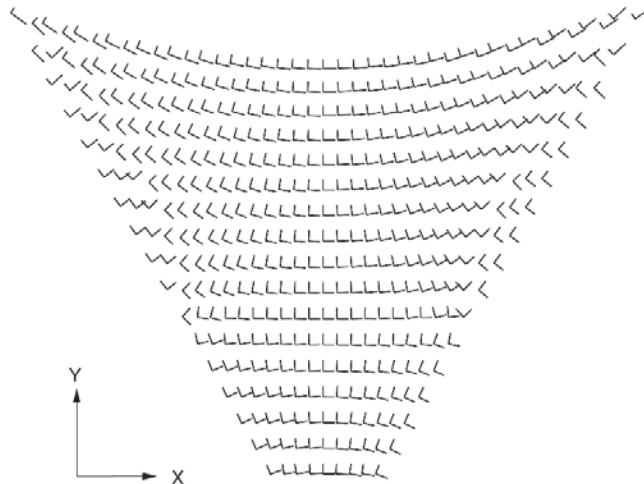


Figure 3.5: Equilibrium surface, direction and magnitude of principal stresses.

3.2.2 Membrane cutting pattern and elastic analysis

For simplicity, it was decided to use a single gore to make a complete one-sixth sector. Because the gore has a central axis of symmetry, the algorithm described in Section 2.5 was used to determine only half of the cutting pattern. The elastic properties of the membrane were set equal to the average values, given in Table 4.1. Thus, the elasticity matrix, Eq. 2.18, has the following expression

$$\mathbf{D} = 10^9 \begin{bmatrix} 13.1 & 3.9 & 0 \\ 3.9 & 13.1 & 0 \\ 0 & 0 & 4.6 \end{bmatrix} \text{ N/m}^2 \quad (3.2)$$

The shape of the cutting pattern is shown in Fig. 3.6. Note that the edge of the pattern looks almost straight: its very small out-of-straightness is the key to achieving the expected shape. Thus, great accuracy is required when the gores are cut and bonded.

After determining the cutting pattern, the elastic analysis of Section 2.6 was carried out. The predicted rms error of the actual reflector turned out to be 3.5 mm, almost unchanged from the rms error of the equilibrium surface. A contour plot of the error of the actual surface is shown in Fig. 3.7.

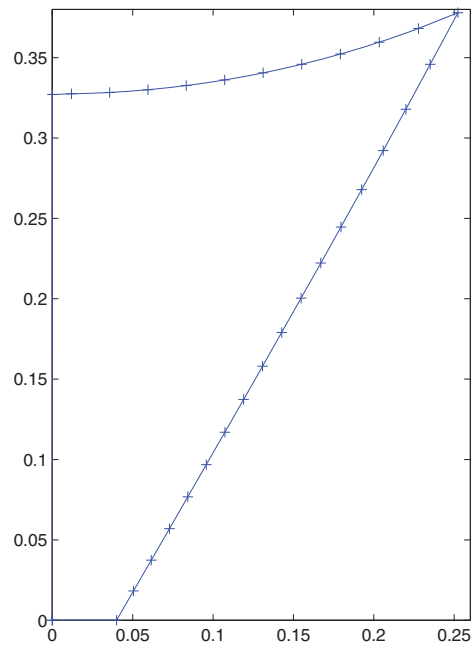


Figure 3.6: Cutting pattern for half gore (dimensions in metres).

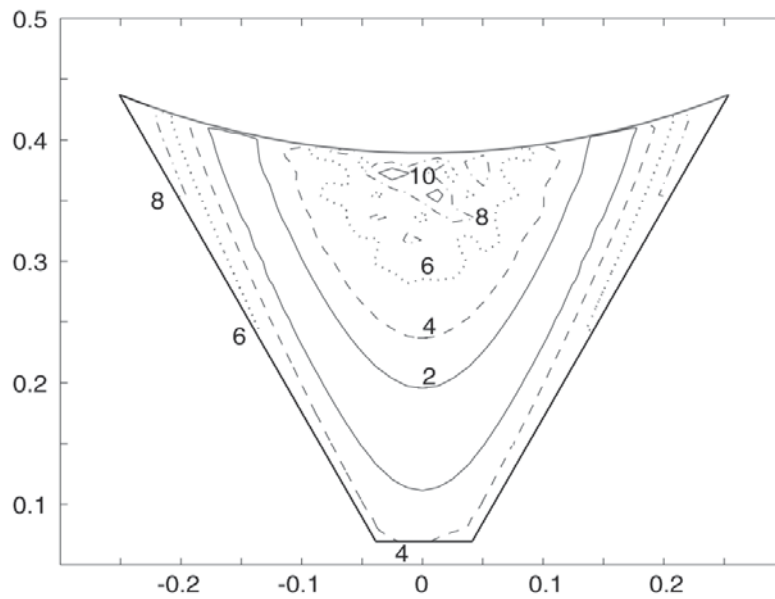


Figure 3.7: Error of actual surface with respect to best fit paraboloid [mm].

A check on the stress distribution in the membrane, however, showed an unexpected problem. Because of the high in-plane stiffness of the Kevlar-reinforced membrane, this membrane requires very high stresses to take up a doubly-curved shape. Hence, the stress distribution that is found at the end of the elastic analysis, shown in Figure 3.8, is vastly different — and with peak value of up to 750 N/m — from the distribution in the equilibrium surface, see Fig 3.5.

It is interesting to examine the stress distribution that is obtained for a much more flexible membrane. If the Kevlar-reinforced Kapton membrane is replaced with a thin Kapton foil the elastic stress distribution, shown in Figure 3.9, is almost identical to the distribution in the equilibrium surface.

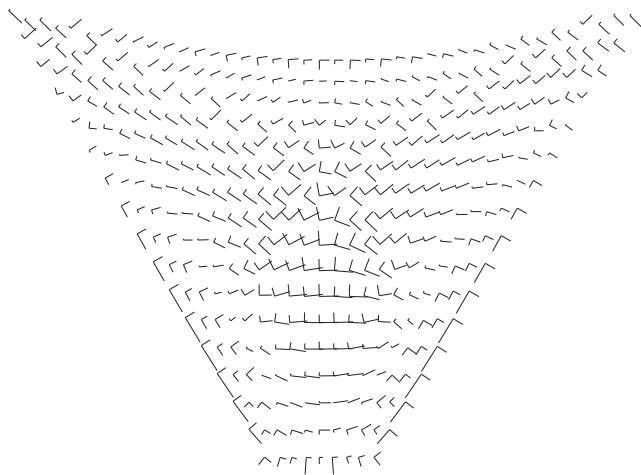


Figure 3.8: Stress distribution in actual surface (Kevlar-reinforced membrane).

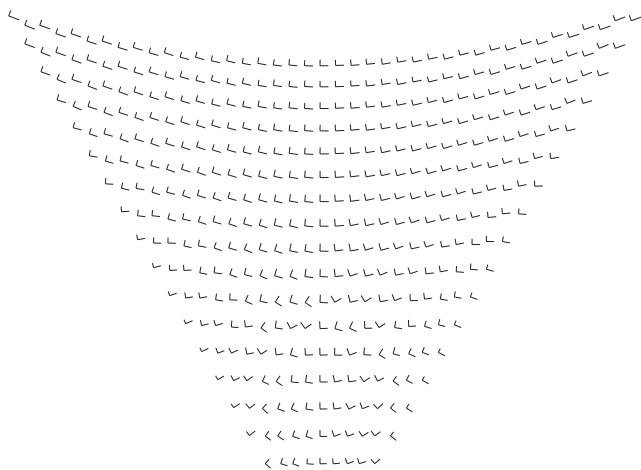


Figure 3.9: Stress distribution in actual surface (0.02 mm thick Kapton membrane).

3.2.3 Rib profile

The unstressed profile of the ribs can be computed once the edge reactions on the membrane are known, see Section 2.7. In the present case, the 17 reaction components have the values listed in Table 3.1.

The rib is divided into 17 beam elements, whose nodes are co-located with the edge nodes of the membrane, whose coordinates were determined at the end of the elastic analysis. The deflection of this beam, due to the nodal forces in Table 3.1 was computed and the deflected shape, shown in Fig. 3.10, coincides with the required unstressed profile of the rib. The values shown are for 0.2 mm thick ribs with radius of 22 mm, subtending an angle of 120°.

Node	(N_X, N_Y, N_Z) [N]
1	(-0.15, 0.0, 0.58)
2	(-0.24, 0.0, 0.70)
3	(-0.34, 0.0, 0.79)
4	(-0.45, 0.0, 0.87)
5	(-0.58, 0.0, 0.93)
6	(-0.71, 0.0, 0.98)
7	(-0.87, 0.0, 1.01)
8	(-1.04, 0.0, 1.02)
9	(-1.23, 0.0, 1.03)
10	(-1.43, 0.0, 1.02)
11	(-1.65, 0.0, 0.99)
12	(-1.88, 0.0, 0.95)
13	(-2.13, 0.0, 0.88)
14	(-2.40, 0.0, 0.79)
15	(-2.69, 0.0, 0.68)
16	(-3.01, 0.0, 0.54)
17	(-144.92, 0.0, -15.13)

Table 3.1: Nodal loads on a rib.

3.3 Analysis of Larger Reflectors

CRTS reflectors of four different apertures and with different numbers of ribs have been analysed in the same way as the 1 m reflector with 6 ribs of Section 3.2. The number of nodes and elements used to model a single gore of each reflector is shown in Table 3.2. The accuracy of the computation is limited by the accuracy with which the mesh of flat elements approximates to a smooth paraboloid, but it would be pointless to aim for an unrealistically high accuracy, by increasing the number of nodes and elements—together with the computational time—excessively. Table 3.3 compares the rms modelling errors of the meshes used. The worst rms error is less than 0.04 mm, in the 1 m diameter model with $n = 6$, way below the target rms errors of this study.

For each reflector configuration that has been analysed, the unweighted and area-weighted rms errors of the reference surface, the equilibrium surface, and the actual

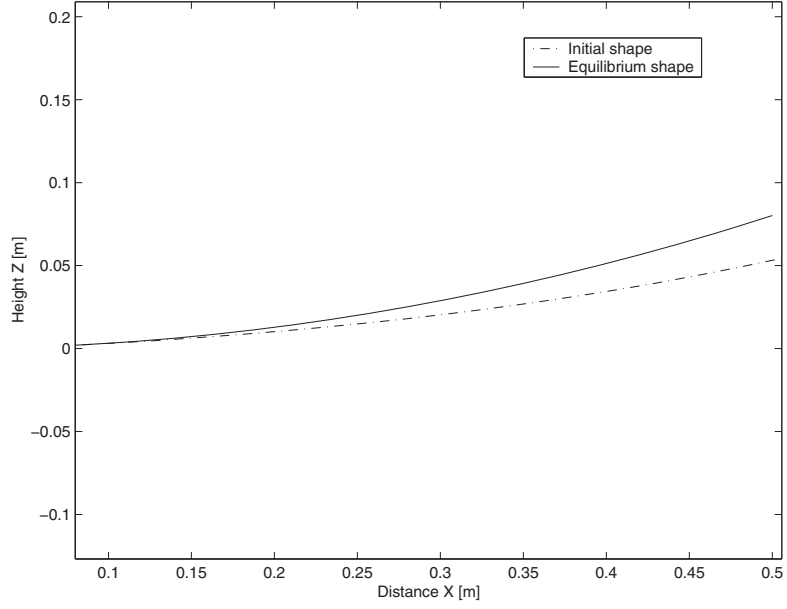


Figure 3.10: Unstressed rib shape.

D [m]	no. of nodes	no. of elements
1	243	425
3	290	513
5	315	560
10	315	560

Table 3.2: Number of nodes and elements in each mesh.

D [m]	n	rms error [mm]
1	6	3.67×10^{-2}
	12	9.79×10^{-3}
	24	2.49×10^{-3}
3	6	1.12×10^{-2}
	12	3.00×10^{-3}
	24	7.65×10^{-4}
5	6	6.47×10^{-3}
	12	1.73×10^{-3}
	24	4.41×10^{-4}
10	6	3.24×10^{-3}
	12	8.67×10^{-4}
	24	2.21×10^{-4}

Table 3.3: Modelling error.

surface are shown in Table 3.4 and Table 3.3, respectively. The tables show that the error difference between the equilibrium and the actual surface is generally small, despite the fact that in all cases a single gore has been used for each sector.

The rms error decreases when the number of ribs is increased, because the reference surface, and hence also the equilibrium and actual surfaces, become closer to the paraboloid. The error increases when the aperture of the reflector is increased.

The rms error of the 1 m diameter with 6 ribs symmetric reflector model is 3.5 mm, which is quite a large value. It may be possible to find a better pre-stress distribution that would lead to a smaller error. A 10 m diameter reflector with 24 ribs, which is perhaps more typical of an actual configuration that might be used for practical applications, is predicted to have an rms error of 4.1 mm.

D [m]	n	Reference surface	Equilibrium surface	Actual surface
1	6	3.3	3.9	3.9
	12	1.0	1.4	1.4
	24	0.3	0.4	0.4
3	6	9.5	11.2	11.3
	12	2.8	4.1	4.1
	24	0.7	1.2	1.2
5	6	15.6	18.6	18.6
	12	4.7	6.7	6.7
	24	1.2	1.9	2.0
10	6	31.1	37.0	37.0
	12	9.3	13.3	13.4
	24	2.4	3.9	4.1

Table 3.4: Unweighted rms errors of reflectors with $F/D = 0.78$ [mm].

D [m]	n	Reference surface	Equilibrium surface	Actual surface
1	6	3.0	3.5	3.5
	12	0.9	1.3	1.3
	24	0.2	0.4	0.4
3	6	8.8	10.5	10.5
	12	2.6	3.9	3.9
	24	0.7	1.2	1.2
5	6	14.7	17.5	17.5
	12	4.3	6.6	6.6
	24	1.1	2.0	2.0
10	6	29.3	35.1	35.1
	12	8.6	13.1	13.1
	24	2.2	3.9	4.1

Table 3.5: Area-weighted rms errors of reflectors with $F/D = 0.78$.

Chapter 4

Experiment Preparation

4.1 Test Article

Figure 4.1 shows a schematic view of the experiment that was set up to compare measurements of prestress and shape for a sector of a small-scale model reflector with the corresponding values predicted by the computational analysis.

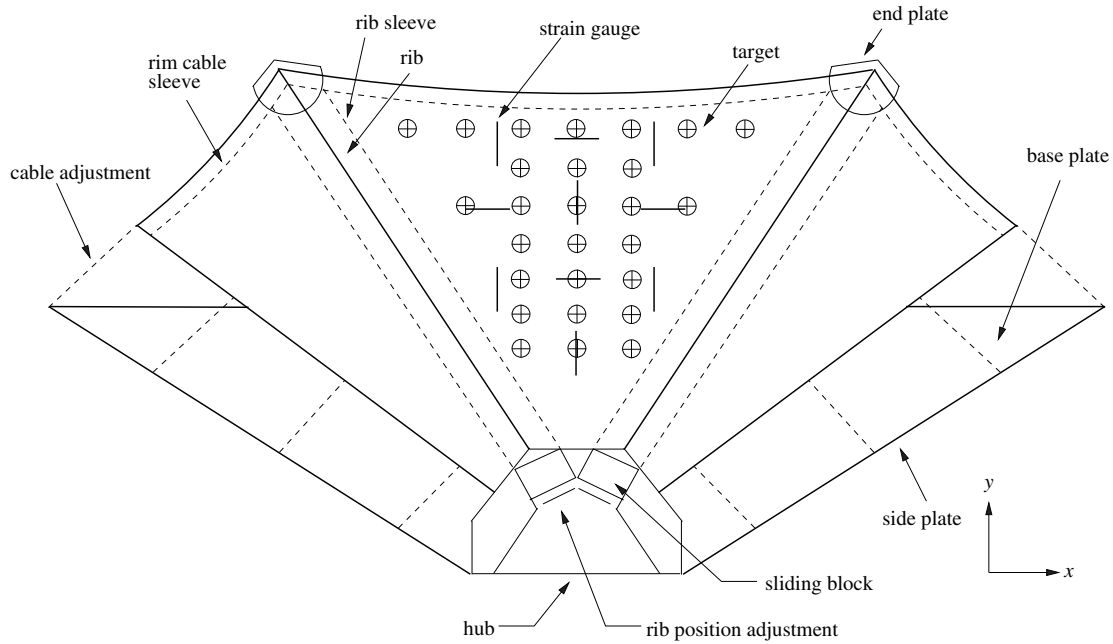


Figure 4.1: Schematic top view of test article.

The model structure is supported by a central hub, fixed to a base plate which supports two side plates that provide two edge supports for the membrane. The membrane consists of a full gore connected to two half gores along the edges. The ribs are accommodated inside membrane pockets lying along the seam between adjacent gores. A series of short cables connect the edge of each half gore to the side plates. By adjusting the tension and the position of these cables, the prestress in the main gore can be adjusted. These side cables simulate the interaction between this gore and its neighbours.

The hub contains two slots in which sliding blocks supporting the ribs can be moved to adjust the level of prestress.

Next, the design and manufacture of the three major components of the experimental model, including the membrane, ribs, and centre hub, will be discussed. Then, the connection details will be explained. Detailed drawings of most components can be found in Appendix B.

4.1.1 Membrane

At an early stage it was decided that it would be desirable to use for the membrane the Kevlar-reinforced Kapton foil previously developed by ESTEC and Contraves in connection with the inflatable, space-rigidised technology. Of course, in the present application the foil would not be impregnated with a self-curing resin. Since Contraves were able to provide for the present study a sufficient amount of the laminate with the smallest amount of fibre reinforcement (LAM8), this foil was used for all experiments. Standard properties for this foil are given in Table 4.1.

Thickness	0.1mm
Density	79 g/m ²
Young's Modulus	11.9×10^9 N/m ²
Poisson's ratio	0.3

Table 4.1: Standard properties of Kevlar-reinforced Kapton foil (see also Section 4.3.1).

As the membrane needs to be cut very precisely, two templates were made from 2 mm thick Al-alloy plate, using a CNC machine, according to the cutting pattern computed in Section 3.2.2. The membrane was laid flat on a soft rubber pad and the templates were clamped on the membrane using G-clamps. The edge profile was cut by hand, using a sharp blade. A magnifying glass was used to ensure precision cutting.

In order to accurately join the main gore to the two half-gores, a plywood mould was made, see Fig. 4.2. The mould is shaped according to the reference surface, and therefore the edges of each gore lie in vertical planes when the gore is laid on this mould. Thus, adjacent gores butt end-to-end when laid on this mould, and can be bonded very accurately. A polyimide adhesive tape was used to bond the gores. Before bonding it to the gores, the tape was peeled off the roll, cut to the required length, and left on a table for several hours to remove all residual strain.

Straight sleeves made from the same membrane were bonded to the gores, with the same tape, along the seam between adjacent gores. The function of these sleeves is to contain the ribs.

4.1.2 Ribs

Copper-beryllium (Cu-Be) and spring steel are two of the materials from which the ribs of a CRTS reflector could be made. Because CuBe can be heat-treated at lower temperature than steel, and also because it had already been used extensively in our laboratory, it was initially planned to make longitudinally curved CuBe ribs for this study. However, the manufacture of the required mould took longer than expected, and

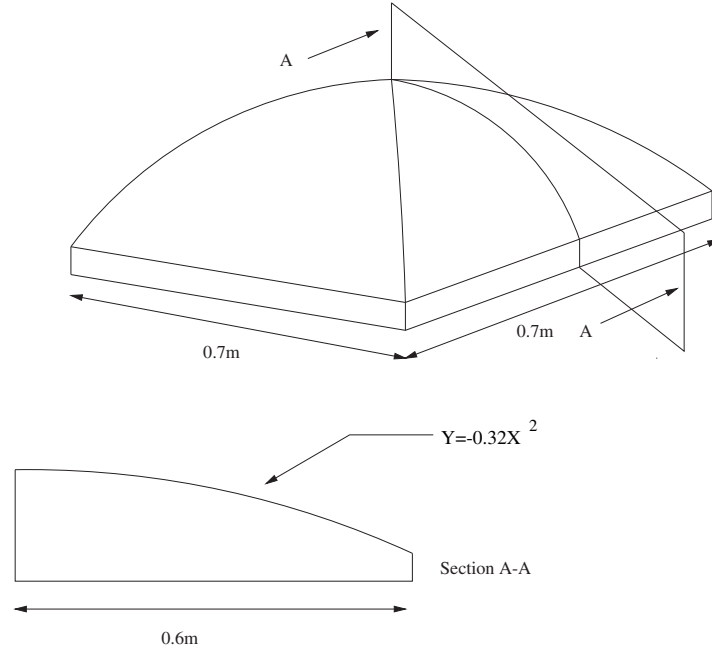


Figure 4.2: Mould on which the gores are bonded.

so it was decided to use straight ribs instead. The idea was to elastically deform these ribs, by lifting them at the tip with spacers, until they reached the required curvature.

It was found that the ribs made by heat-treatment of CuBe sheet using the same mould that had been made for a previous study of CRTS reflectors (You and Pellegrino 1994) were not suitable for this experiment, as they buckle before the required curvature has been reached. It was also found that standard Stanley Galaxie tape measure, whose cross-section subtends a smaller angle than the CuBe ribs —see Fig. 4.3— can be bent to a much larger curvature without buckling. The properties of both the heat treated Cu-Be rib and the steel tape-measure are compared in Table 4.2.

Figure 4.4, produced by finite element analysis (Seffen and Pellegrino 1997), shows that the Cu-Be rib buckles at around 0.35 rad, which is lower than the required end rotation, 0.36 rad. On the other hand, the tape-measure buckles at an end rotation of 0.89 rad which leaves plenty of room for adjusting the configuration of the membrane without buckling the rib.

4.1.3 Hub

The hub was machined from a solid block of mild steel. Two slots at an angle of 60° , which is the angle subtended by a one-sixth sector of the full reflector, were machined to allow the blocks supporting the ribs to move back and forth.

An adjustment block, also made of mild steel, slots into the hub behind the ribs and is attached to the hub by screws. Two caphead screws, coaxial with these slots, are used to adjust the position of the rib sliding blocks.

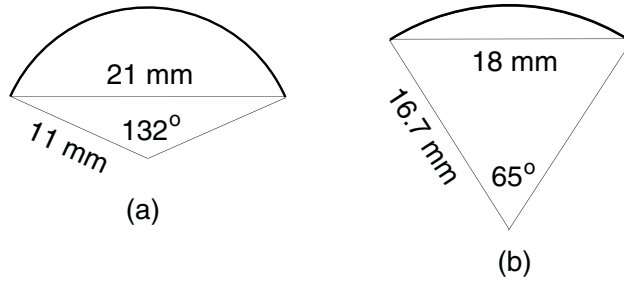


Figure 4.3: Rib cross-section.

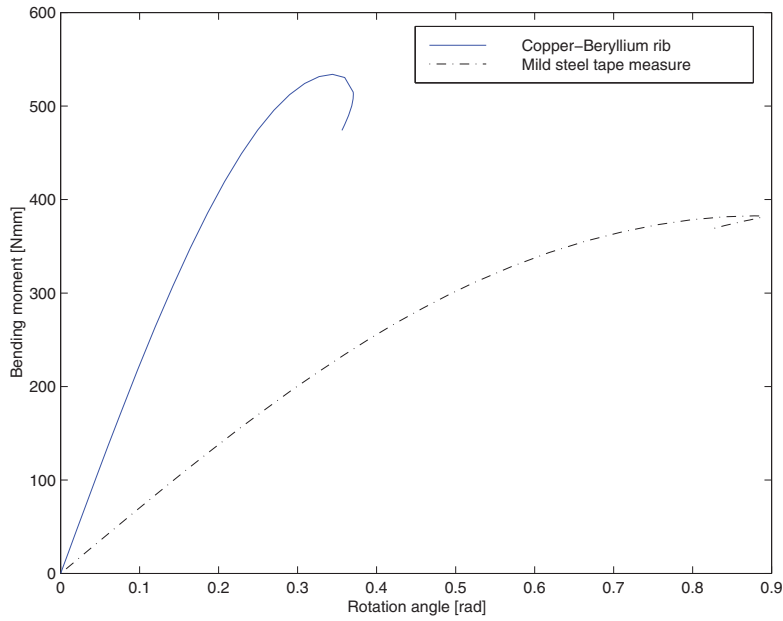


Figure 4.4: Moment/rotation relationship for a rib.

Material	Copper-Beryllium	Steel tape measure
Density	$8.4 \times 10^3 \text{ kgm}^{-3}$	$7.8 \times 10^3 \text{ kgm}^{-3}$
Young's Modulus	$131 \times 10^9 \text{ Nm}^{-2}$	$210 \times 10^9 \text{ Nm}^{-2}$
Transverse radius	11 mm	16.7 mm
Subtended angle	132°	65°
Thickness	0.1 mm	0.15 mm
Length	530 mm	530 mm
Stiffness EI	1.27 Nm^2	0.41 Nm^2

Table 4.2: Rib properties.

4.1.4 Connections

The root of each rib was glued into an Al-alloy sliding block, Fig. 4.5. The tip of the rib was fixed to a 0.5 mm thick shim steel plate, which was connected to the rib by a screw, through a steel washer with a curved upper surface. Slots on either side of the plate permit a small adjustment of the cable connectors, to adjust the length of the Kevlar 49 edge cable, Fig. 4.6. The attachments are made with specially made hollow screws that accommodate the cables inside, see Fig. 4.7. Note that the cable can be tensioned by turning the connector, but does not twist.

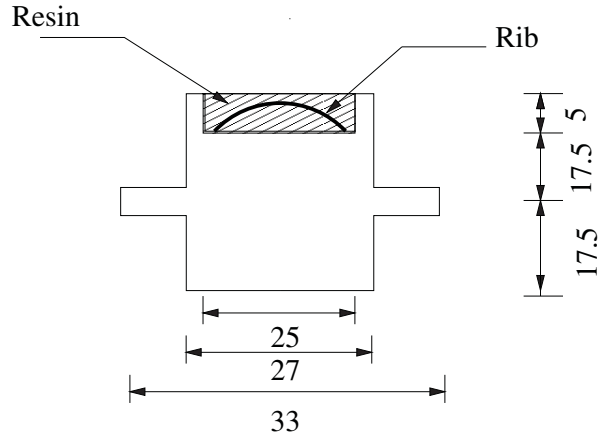


Figure 4.5: Cross-section of rib sliding block.

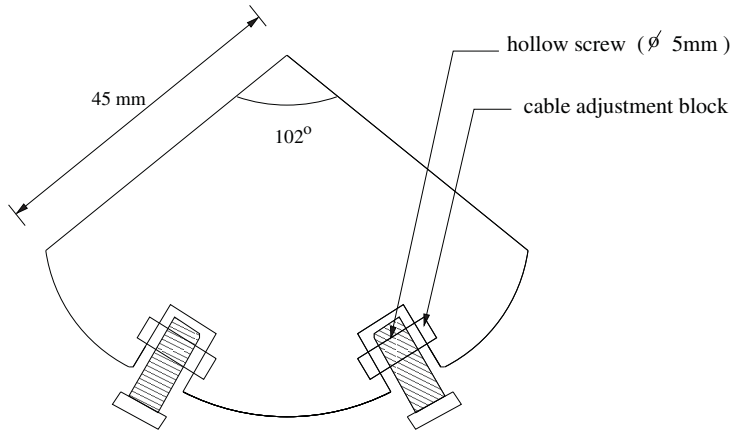


Figure 4.6: End plate.

The six cables that connect the two side gores, through strips of shim steel, to vertical slots in the side plates, contain turn-buckles similar to the cable connectors in Fig. 4.7.

The outer edge of each gore is tensioned by a cable contained within a sleeve formed by folding the membrane on itself and taping it with adhesive tape.

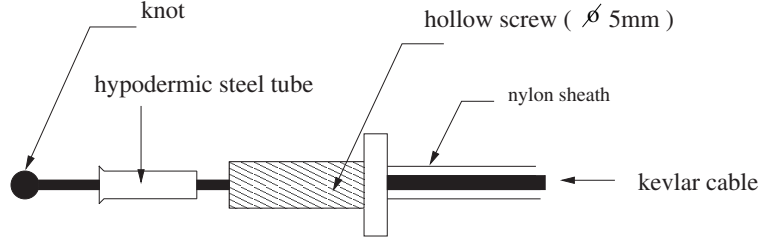


Figure 4.7: Edge cable connector.

4.2 Measurement Methods

The strain in the membrane was measured by means of strain gauges directly glued to the Kapton foil. The shape of the membrane was determined by measuring the three-dimensional coordinates of small targets glued on the membrane, with an industrial measurement system consisting of three electronic theodolites.

4.2.1 Strain measurements

It is often argued that measuring strain in a thin membrane by means of strain gauges is not accurate because (i) the glue used to stick the strain gauges onto the membrane stiffens the membrane locally, and (ii) the thermal strain induced by the strain gauge significantly distorts the readings. However, since it would have been difficult to obtain accurate measurements of strain in the reflector membrane with any other method, at a reasonable cost, it was decided to make a more careful study of the viability of using strain gauges. It was found that quite accurate and stable measurements can be made if *large strain gauges* (approximately 30 mm long) are used in a *thermally stable environment*.

Ten strain gauges were glued to the membrane, at the locations shown in Fig. 4.8; note the additional gauge for thermal compensation. The coordinates of the centre of each gauge are listed in Table 4.3.

All the strain gauges were connected to a data acquisition system (Microlink 3000), which has similar functions to a normal data logger, and the system was connected to a personal computer running Labview, a program for experimental data analysis. The advantage of using this system is that the strains can be monitored and plotted on line while carrying out an experiment, so that any anomalies can be easily spotted. A disadvantage of this system is that it energises the strain gauges continuously, thus heating the membrane. However, it was found that the readings are reasonably stable if the system is left on for several hours before doing an experiment, so that the temperature of all the strain gauges remains constant, and if the experiment is carried out in a constant-temperature room. Also, a Perspex cover box was made around the membrane surface, to reduce the air flow around it.

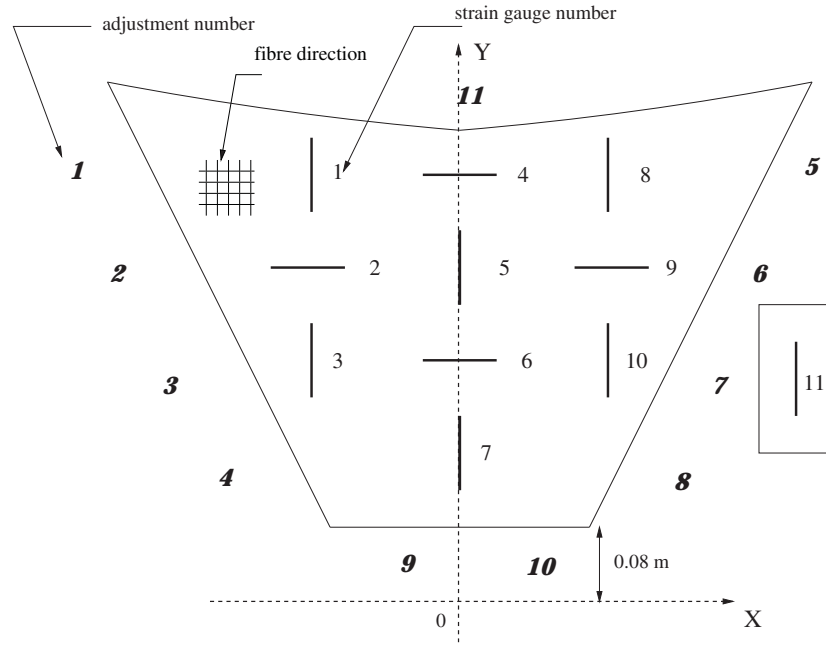


Figure 4.8: Layout of strain gauges and numbering of adjustments.

Strain gauge	(X,Y) [m]
1	(-0.07, 0.34)
2	(-0.07, 0.27)
3	(-0.07, 0.21)
4	(0.00, 0.34)
5	(0.00, 0.26)
6	(0.00, 0.21)
7	(0.00, 0.17)
8	(0.07, 0.34)
9	(0.07, 0.27)
10	(0.07, 0.21)

Table 4.3: Position of strain gauges in the coordinate system of Fig. 4.8.

Due to thermal drift, it is impossible to measure the strains in the membrane to an accuracy greater than ± 10 micro-strain. Hence an experimental error of $\pm 5\%$ can be expected.

4.2.2 Shape measurements

Once the correct stress/strain distribution had been achieved in the membrane, its shape was measured using three Zeiss ETh2 electronic theodolites. These theodolites are connected to a personal computer which analyses the angular readings from the theodolites and determines the 3D coordinates of any points within a triangular region whose vertices coincide with the theodolites (Kwan and You 1993).

The theodolites are labelled 1, 2 and 3 in an anti-clockwise direction. The reference coordinate system is defined so that the origin of the coordinate system is at the centre of Theodolite 1, the Z-axis is the vertical axis, and Theodolite 2 is in the X-Z plane. All three theodolites must be initialised and calibrated before taking any measurement, although it is possible to measure coordinates of a point which is visible only from two theodolites.

The measurement of the coordinates of a point involves three unknowns, but there are normally six angular readings, if three theodolites are used, hence six independent equations are available. This is an over-determinate situation. An iterative least-squares calculation is carried out to give the 'best' set of coordinates to satisfy all six equations. Average coordinates of the observed point, calculated by simple triangulations, serve as both initial values for the iteration and a check that the three theodolites are all pointing roughly towards the same point.

Kwan and You (1993) have shown that an accuracy of the order of ± 0.1 mm can be obtained with this measurement system.

4.3 Material Properties

To verify that the material properties assumed in the design of the experiment were sufficiently close to their actual values, and also to validate the technique for measuring strains in the membrane using strain gauges, tension tests were carried out on the membrane, on the tape-measure, and on two pieces of membrane connected by polyimide tape.

4.3.1 Membrane

Kevlar-reinforced Kapton foil is not an isotropic material, as the fibres are woven in two perpendicular directions. Its elastic properties have been characterised by Oerlikon-Contraves (1993) using a photogrammetric technique. Their values are given in Table 4.4, where x and y denote the fibre directions.

Despite the considerable efforts made to achieve accurate results, the authors of this report concluded that "the application of the transverse load precludes the determination of the Poisson's ratio for LAM25 and calls into question the validity of the results obtained for LAM8." It should be noted that the measured Poisson's ratios values are higher than would be expected in a two-dimensional lamina reinforced by straight fibres and, furthermore, the measured values do not satisfy the reciprocity relationship

$$\frac{\nu_{xy}}{E_x} = \frac{\nu_{yx}}{E_y} \quad (4.1)$$

Finally, the full characterisation of an orthotropic lamina requires four independent elastic constants (Gibson 1994), but the value of G_{xy} was not measured.

Loading N/m	$E_x h$ [MN/m]	$E_y h$ [MN/m]	ν_{xy}	ν_{yx}
100	1.18 ± 0.34	0.83 ± 0.14	0.46	0.49
200	1.1 ± 0.21	0.76 ± 0.13	0.32	0.36

Table 4.4: Elastic moduli of Kevlar-reinforced Kapton foil (Oerlikon-Contraves 1993).

Using the known elastic constants, the following relationships can be set up between force per unit width, σ_{xx} , etc. predicted by our computational analysis, and the linear strain components in the membrane, which are measured by the strain gauges

$$\begin{aligned} \epsilon_{xx} &= \frac{\sigma_{xx} h}{E_x h} - \nu_{yx} \frac{\sigma_{yy} h}{E_y h} \\ \epsilon_{yy} &= -\nu_{xy} \frac{\sigma_{xx} h}{E_x h} + \frac{\sigma_{yy} h}{E_y h} \end{aligned} \quad (4.2)$$

To obtain independent estimates of E_x, E_y —and thus validate our technique for measuring strains in the membrane— a series of tension tests were carried out on three 250 mm long membrane strips, cut at angles of $0^\circ, 45^\circ$ and 90° from a single piece of foil. A dead-weight loading arrangement was used, to eliminate friction and uncontrolled loads on the membrane, see Fig. 4.9. Because the prestress level in the experiment is around 200 N/m, the maximum loading applied was 300 N/m. Both loading and unloading were carried during these tests.

Sample results from these tests are shown in Fig. 4.10. The Young’s Moduli estimated from the present test are compared to the results obtained by Oerlikon-Contraves (1993) in Table 4.5. Our results are within the experimental error of the previous values. This shows that our simple approach for measuring the strains in the membrane reflector, by means of strain gauges, is acceptable. Our experiments have also shown that the response of the membrane is almost linear.

Figure 4.10c suggests that Kevlar-reinforced Kapton foil has a rather low shear modulus, whose value will need to be measured by repeating this test with an additional strain gauge, at 90° to the direction of loading.

	Present experiment		Oerlikon-Contraves	
Loading N/m	$E_x h$ MN/m	$E_y h$ MN/m	$E_x h$ MN/m	$E_y h$ MN/m
100	1.03	0.67	1.18 ± 0.34	0.83 ± 0.14
200	1.04	0.61	1.1 ± 0.21	0.76 ± 0.13

Table 4.5: Elastic moduli of membrane.

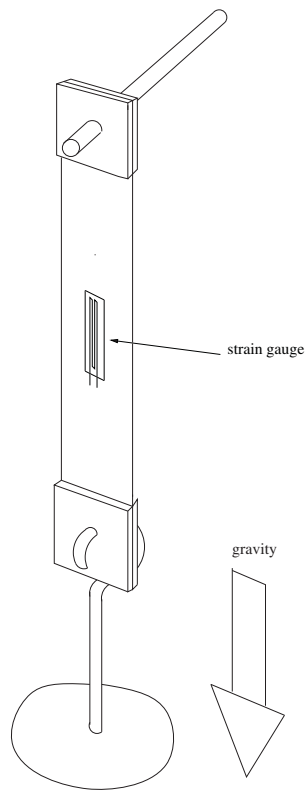
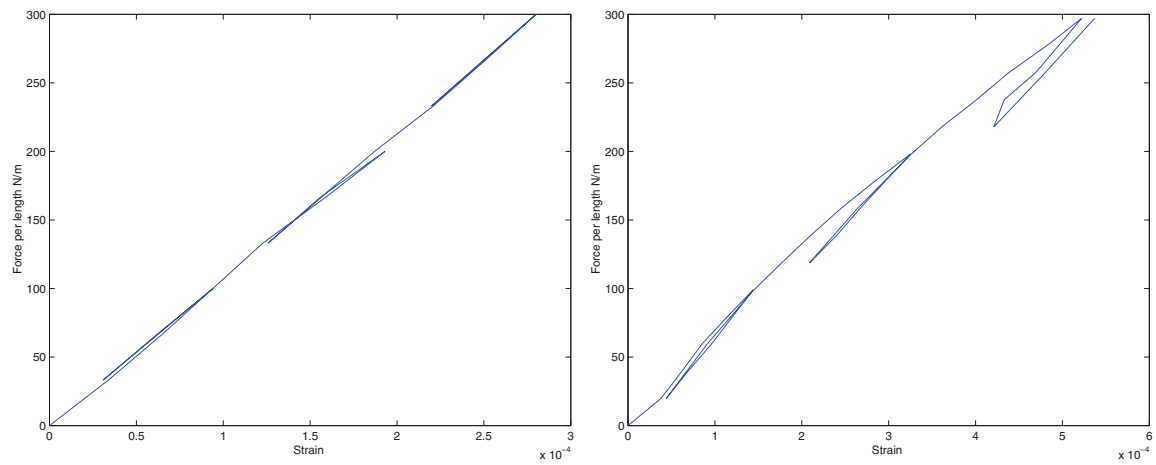
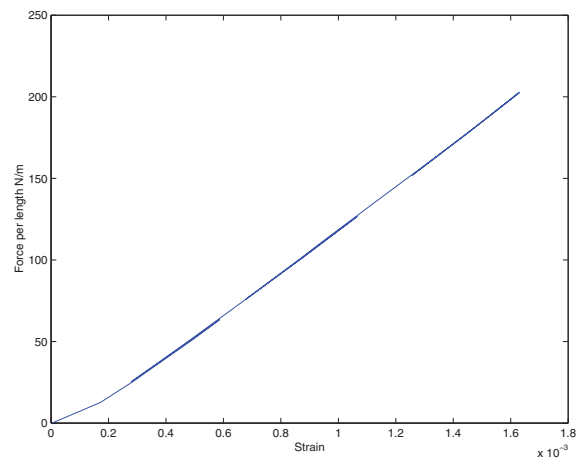


Figure 4.9: Schematic layout of tension test on membrane strip.



(a) load in x -direction

(b) load in y -direction



(c) load at 45° to x and y

Figure 4.10: Tension tests on membrane strips.

4.3.2 Ribs

A tension test was done on a 200 mm length of Stanley Galaxie tape measure, using a Hounsfield Tensometer. The strain in the tape was measured with a strain gauge glued to its surface. The Young's Modulus was measured to be $210 \times 10^9 \text{ N/m}^2$.

4.3.3 Adhesive tape

The strength of the connection between two gores bonded with this tape was measured by carrying out several tension tests with the layout of Fig. 4.9. It was found that the connection fails under a load of 1500 N/m, which is about seven times the intended loading of the membrane during the experiment. Also, the connection tends to creep if loads are left on for a few hours. Therefore, it was decided that the model should not be left prestressed overnight.

Chapter 5

Experimental Results

5.1 Prestress Adjustment

The initial plan was to carry out a preliminary adjustment of the prestress in the membrane that would take the measured strains as close as possible to the values that correspond to a uniform biaxial prestress of $sh=[170, 170, 0]$ N/m, i.e. $\mathbf{e}=[63, 226, 0]$. Then, a relationship would be set up between the adjustments and the strains, by measuring the strain changes after each adjustment had been turned by one unit, i.e. 360° . For example, when the adjustment screw 1, q_1 , is turned through 360° , the changes of strain in the gauges are $a_1^1, a_2^1, \dots, a_{10}^1$, and so on. Thus, setting up an adjustment matrix

$$\begin{bmatrix} a_1^1 & a_1^2 & \dots & a_1^{11} \\ a_2^1 & a_2^2 & \dots & a_2^{11} \\ \vdots & \vdots & & \vdots \\ a_{10}^1 & a_{10}^2 & \dots & a_{10}^{11} \end{bmatrix} \begin{bmatrix} q_1 \\ q_2 \\ \vdots \\ q_{11} \end{bmatrix} = \begin{bmatrix} de_1 \\ de_2 \\ \vdots \\ de_{10} \end{bmatrix} \quad (5.1)$$

Defining an adjustment vector, \mathbf{q} , and a strain change vector, $d\mathbf{e}$, equal to the difference between the desired strain levels and the current measured strains, Eq. 5.1 can be written as

$$\mathbf{A}\mathbf{q} = d\mathbf{e} \quad (5.2)$$

Note that Eq. 5.2 is over-determinate, and hence has to be solved by least squares.

Following this plan, several calibration experiments were carried out to find the relationship between adjustments and strain changes. For each adjustment, a graph of the strain changes against the number of turns in the screw was plotted. It showed that the relationship was never exactly linear, but a straight line was fitted to the measured values, and the gradient of this line provided one of the entries of the matrix \mathbf{A} . Once the complete matrix had been obtained, it was used to compute the required adjustments for the strain corrections, but it was found that the strains at gauges 3, 5, 7 and 10, see Fig. 4.8, never became even close to the expected values. Therefore, it was decided to exclude from the experiment the readings from gauges 3, 5, 7 and 10.

It was also found that the adjustment matrix is not exactly the same in different experiments because the prestress level is different, but an example of a measured adjustment matrix is given here

$$A = \begin{matrix} & q^1 & q^2 & q^3 & q^4 & q^5 & q^6 & q^7 & q^8 & q^9 & q^{10} & q^{11} \\ \begin{matrix} d\epsilon_1 \\ d\epsilon_2 \\ d\epsilon_4 \\ d\epsilon_6 \\ d\epsilon_8 \\ d\epsilon_9 \end{matrix} & \begin{pmatrix} 4.7 & -1.7 & 1.0 & 6.5 & 7.2 & 3.4 & 1.8 & 4.3 & 41.5 & 29.1 & -16.4 \\ -0.2 & 1.8 & 10.8 & 16.4 & 5.1 & 6.4 & 6.2 & 37.8 & 37.8 & 40.0 & -29.4 \\ 4.8 & 8.9 & 12.8 & 6.1 & 3.0 & 7.8 & 15.2 & 6.2 & 53.6 & 32 & -9.2 \\ -11.4 & -11.1 & 7.6 & 20.0 & 3.7 & 14.0 & 18.3 & -3.0 & 34.4 & 33.6 & -3.32 \\ 5.2 & 5.6 & 5.1 & 7.6 & 5.6 & 1.0 & 2.4 & 5.6 & 14.0 & 20.0 & 5.6 \\ -4.2 & -2.4 & 2.0 & 16.8 & 4.6 & 17.8 & 18.6 & 1.8 & 4.8 & 35.0 & -17.5 \end{pmatrix} \end{matrix} \quad (5.3)$$

Note that the most effective adjustments are 9, 10 and 11, where a full turn changes the average strain by about 30 micro-strain, but the side adjustments tend to be much less effective.

Table 5.1 shows a set of initial measurements that were taken. To achieve the required corrections, Eq. 5.1 predicts the following adjustments

$$\mathbf{q} = [1.8 \quad 3.9 \quad -0.9 \quad -11.2 \quad -1 \quad 1.9 \quad 1.9 \quad 6.4 \quad 7.1 \quad -0.9 \quad 13.5 \quad 6.8]^T$$

The largest adjustment, q_4 , should be turned 11 times, but this cannot be done because the membrane would lose tension.

It has been found that this is a general problem with this approach. Because Eq. 5.1 assumes that the membrane can carry both tension and compression, it often produces an “exact” answer which physically cannot be realised. Another problem is that several times during our experiments, the ribs have suddenly buckled in the middle of an adjustment sequence, so that the experiment had to be re-started.

Strain Gauge	Expected strain	Current strain
1	64	82
2	160	100
4	212	103
6	184	128
8	120	90
9	160	76

Table 5.1: Strain measurements [micro-strains].

To resolve these difficulties, it was decided to use the matrix \mathbf{A} only as a guideline, instead of using directly the adjustments that it predicts. Thus, by a trial and error approach, a series of iterative adjustments were carried out until the strains reached the values listed in Table 5.2. In this particular experiment the average error decreased from 39% to 22%.

Strain Gauge	Expected strain	Initial strain	Error	After first adjustment	...	Final strain	Error
1	64	80	-25%	82	...	75	-19%
2	160	105	34%	120	...	125	22%
4	212	124	41%	180	...	170	20%
6	184	38	79%	92	...	153	-17%
8	64	42	34%	85	...	82	-28%
9	160	121	24%	101	...	113	29%

Table 5.2: Strain adjustment sequence [micro-strains]

5.2 Shape Measurement

Once the strains had been adjusted, the shape of the surface was measured. It was decided to measure only the coordinates of the 26 target points shown in Fig. 5.1, in the centre of the gore, because near the hub the shape accuracy is affected by the existence of a gap between the hub and the membrane and near the ribs it is affected by the rib-sleeve connection.

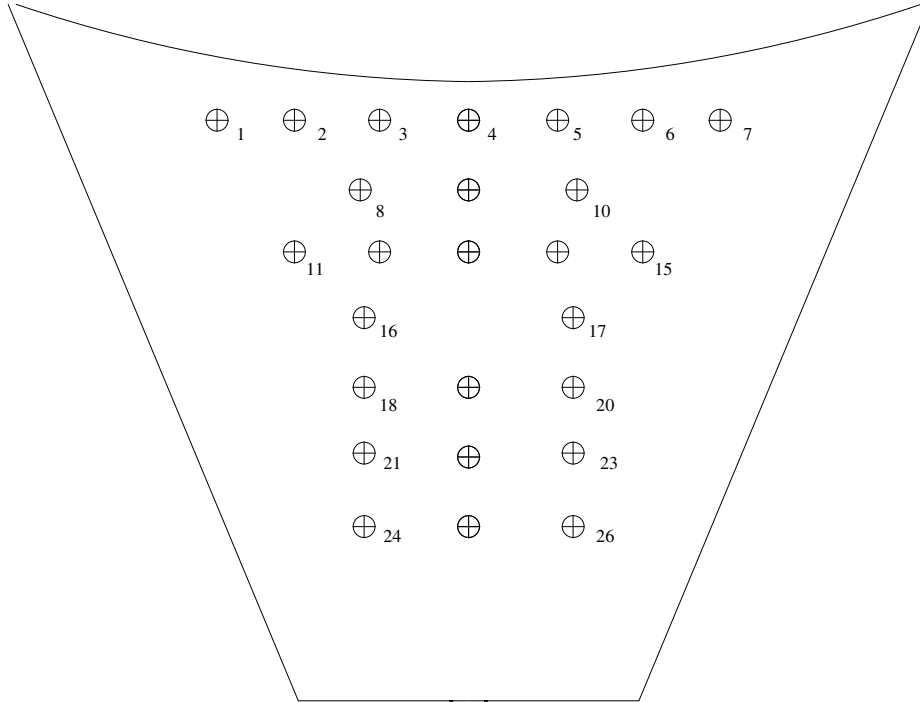


Figure 5.1: Target points on the surface model.

The measured coordinates of each target point are given in Table 5.2. These coordinates are relative to the coordinate system defined by the theodolites, see Section 4.2.2.

The equation of the best-fit paraboloid, computed from Eq. A.6, is

Target Point	(X,Y,Z) [m]
1	(0.8609, 0.5897, -0.6251)
2	(0.8800, 0.5578, -0.6252)
3	(0.9018, 0.5233, -0.6251)
4	(0.9207, 0.4931, -0.6253)
5	(0.9431, 0.4601, -0.6247)
6	(0.9617, 0.4291, -0.6251)
7	(0.9824, 0.3980, -0.6258)
8	(0.8792, 0.5099, -0.6331)
9	(0.8979, 0.4785, -0.6330)
10	(0.9195, 0.4461, -0.6330)
11	(0.8354, 0.5294, -0.6409)
12	(0.8561, 0.4964, -0.6405)
13	(0.8752, 0.4647, -0.6407)
14	(0.8954, 0.4324, -0.6404)
15	(0.9169, 0.4013, -0.6408)
16	(0.8336, 0.4817, -0.6474)
17	(0.8734, 0.4181, -0.6476)
18	(0.8097, 0.4670, -0.6557)
19	(0.8297, 0.4355, -0.6553)
20	(0.8517, 0.4009, -0.6550)
21	(0.7898, 0.4538, -0.6610)
22	(0.8089, 0.4225, -0.6610)
23	(0.8284, 0.3889, -0.6615)
24	(0.7692, 0.4409, -0.6659)
25	(0.7879, 0.4092, -0.6654)
26	(0.8083, 0.3764, -0.6654)

Table 5.3: Coordinates of target points.

$$Z = 0.1034(X^2 + Y^2) + 0.0421X + 0.0456Y - 0.8003 \quad (5.4)$$

and the corresponding unweighted rms error is 0.7 mm. This value is much smaller than the error of 3.5 mm that was given in Table 3.4. However, these two values cannot be compared because one refers to about half of a gore, while the other refers to the complete gore. A new theoretical estimate was made for approximately the same region covered by the targets and the unweighted rms error was found to be 1.9 mm. This value is closer to the experimental value, which at first may seem a rather pleasing result. However, it should be noted that this is a *much flatter paraboloid* than that aimed for, c.f. Equation 3.1.

Chapter 6

Conclusion

6.1 Discussion

The shape and stress analysis of a CRTS reflector have been investigated, both analytically and experimentally.

The analytical part of the study has established a methodology for the preliminary design of this type reflectors, as follows. Given the aperture diameter, focal length, and target rms error, as well as the maximum permissible ratio between the highest and lowest principal stress in the membrane, the key stages of the design process are as follows.

- Determination of the required number of ribs n using the concept of a *reference surface*.
- Computation of the *equilibrium surface*, i.e. a surface whose rms error is better than the prescribed limit, and which is in equilibrium under an acceptable state of prestress.
- Computation of the cutting pattern.
- Verification that the shape and distribution of prestress in a membrane made according to the computed pattern satisfy all the stated requirements.
- Computation of the unstressed profile of the ribs.

Estimates have been made of the rms error of reflectors with apertures of 1, 3, 5, and 10 m, with 6, 12, and 24 ribs. It has been found that the error that can be expected in a reflector is typically 50% greater than the error in the reference surface for the same reflector. This provides a simple way of making preliminary estimates.

The experimental part of the study has compared the measurements of prestress and shape in a one-sixth sector of a 1 m diameter reflector with 6 ribs, with predictions obtained from the computational study.

The initial aim of the experiments had been to investigate the feasibility of setting up a biaxially prestressed surface that approximates closely to a paraboloid of a given equation. This was unsuccessful, as it might have been expected by noticing that the high in-plane stiffness of Kevlar-reinforced Kapton is so high that the only configuration of the membrane in which a biaxial state of prestress can be in equilibrium is one in

which the membrane is flat. Hence, at the end of the experiments it was realised that the prestress adjustment sequence had gradually achieved a locally flat configuration of the membrane.

It was thus realised that, since an initially curved membrane was not available, the only possible option was to aim for a nearly unidirectional stress distribution along the membrane surface.

The following specific conclusions can be drawn from the present study:

- The computational modelling of the reflector by using force-density method works well.
- The most effective way of adjusting the stress distribution in a gore is to move the supporting ribs and to vary the length of the cable running along the outer edge.
- The simple method of measuring the stress in the membrane by using strain gauges provides acceptable accuracy, provided that large strain gauges are used and that the measurements are conducted in a thermally stable environment.

6.2 Recommendations

It is recommended that the following aspects be further considered and/or investigated.

- Larger experimental models should be used in future experiments.
- Curved ribs should be used.
- The behaviour of the membrane material under non-uniform biaxial stress needs to be investigated.
- The use of nearly-isotropic foils should be considered, such as Kapton reinforced with a triaxial weave of Kevlar.

6.3 Acknowledgements

We thank the Project Manager, Mr W.J. Rits, for technical advice and support. Assistance with the experiments has been provided by our colleagues Mr R.D. Denston, Mr D. Green and Mr P.J. Knott. The membrane used for the experiments was kindly supplied by Oerlikon-Contraves. Financial support from EPSRC, in the form of an Advanced Research Fellowship for Dr You, is gratefully acknowledged.

Appendix A

Computation of rms error

The surface accuracy of a reflector antenna is an important parameter to estimate its electro-magnetic performance, because surface distortion causes undesirable phase shifts of the microwave radiation, thus reducing the gain of the reflector. Here, the relevant measure of surface accuracy is the root mean square (rms) of half the difference between the path lengths of microwave beams travelling from the deformed surface to the focus, and the corresponding path lengths for a perfect paraboloid. This error is denoted by δ .

Note that it is not the absolute distortion of the surface that affects the performance of the antenna, but its relative distortion. For example, a “distortion” pattern consisting of a rigid-body displacement of the whole reflector leaves the performance unaffected, provided that the antenna feed is also displaced. Therefore, the rms surface error is not computed with respect to the design paraboloid, but with respect to the *best fit paraboloid*, i.e. that special paraboloid which produces the minimum rms error.

According to the standard theory by Ruze (1966) the gain reduction, expressed as the ratio between the actual gain of an antenna and the gain of a similar, but undistorted antenna, is related to the radiation wavelength, λ , by

$$\eta_s = e^{-(4\pi\delta/\lambda)^2} \quad (\text{A.1})$$

From this expression it can be seen that the antenna gain sharply decreases as δ increases.

For non-shallow reflectors, that is reflectors with small values of F/D (F = focal length and D = aperture diameter), the effective rms surface error δ that is used in Eq. A.1 is related to δz , the rms error measured in the axial direction, by (Ruze 1966)

$$\delta = \frac{\delta z}{1 + (D/4F)^2} \quad (\text{A.2})$$

For a reflector surface that is represented by a discrete set of target points, such as the nodes of a finite-element of the surface (Levy 1996), the computation of the rms error is carried out as follows. Let $(X_1, Y_1, Z_1), \dots, (X_n, Y_n, Z_n)$ be the coordinates of n target points that are *equally spaced on the surface*. With respect to its own coordinate system, see Fig. A.1, the equation of the best-fit paraboloid is of the type

$$z = a(x^2 + y^2) \quad (\text{A.3})$$

Converting to the coordinate system in which the measurements were taken

$$\begin{aligned} x &= X - X_0 \\ y &= Y - Y_0 \\ z &= Z - Z_0 \end{aligned}$$

and, substituting into Eq. A.3

$$Z = a(X^2 + Y^2) - 2aX_0X - 2aY_0Y + X_0^2 + Y_0^2 + Z_0 \quad (\text{A.4})$$

this equation contains four unknown parameters, a , X_0 , Y_0 , and Z_0 . Defining a more convenient set of unknowns, it can be written in the form

$$Z = a(X^2 + Y^2) + bX + cY + d \quad (\text{A.5})$$

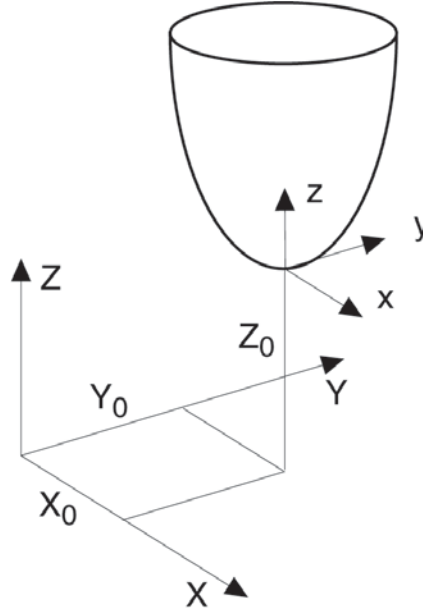


Figure A.1: Position of best-fit paraboloid with respect to theodolite coordinate system.

Substituting the n sets of target coordinates into Eq. A.5 we set up the following over-determinate system of linear equations, containing n equations but only four unknowns

$$\begin{bmatrix} (X_1^2 + Y_1^2) & X_1 & Y_1 & 1 \\ (X_2^2 + Y_2^2) & X_2 & Y_2 & 1 \\ \dots & \dots & \dots & \dots \\ (X_n^2 + Y_n^2) & X_n & Y_n & 1 \end{bmatrix} \begin{bmatrix} a \\ b \\ c \\ d \end{bmatrix} = \begin{bmatrix} Z_1 \\ Z_2 \\ \dots \\ Z_n \end{bmatrix} \quad (\text{A.6})$$

which can be written as

$$A\alpha = \beta \quad (\text{A.7})$$

The least squares solution of Eq. A.7 (Strang 1980) is given by

$$\hat{\alpha} = (A^T A)^{-1} A^T \beta \quad (\text{A.8})$$

where $\hat{\alpha}$ contains the coefficients of the best fit paraboloid. Then, having noted that $A\hat{\alpha}$ is the vector that contains the Z -coordinates of the points on the best-fit paraboloid that approximate the original target points, the rms error in the axial direction is given by

$$\delta Z = \sqrt{\frac{s \sum (\hat{Z}_i - Z_i)^2}{S}} = \frac{\|A\hat{\alpha} - \beta\|}{\sqrt{n}} \quad (\text{A.9})$$

where S is the total surface area of the reflector and $s = S/n$ is the surface area associated with each node. Equation A.9 can be readily modified if different surface areas s_i are associated with different nodes, and this can also be taken into account by introducing weights s_i/S in Eq. A.7.

Appendix B

Manufacturing Drawings

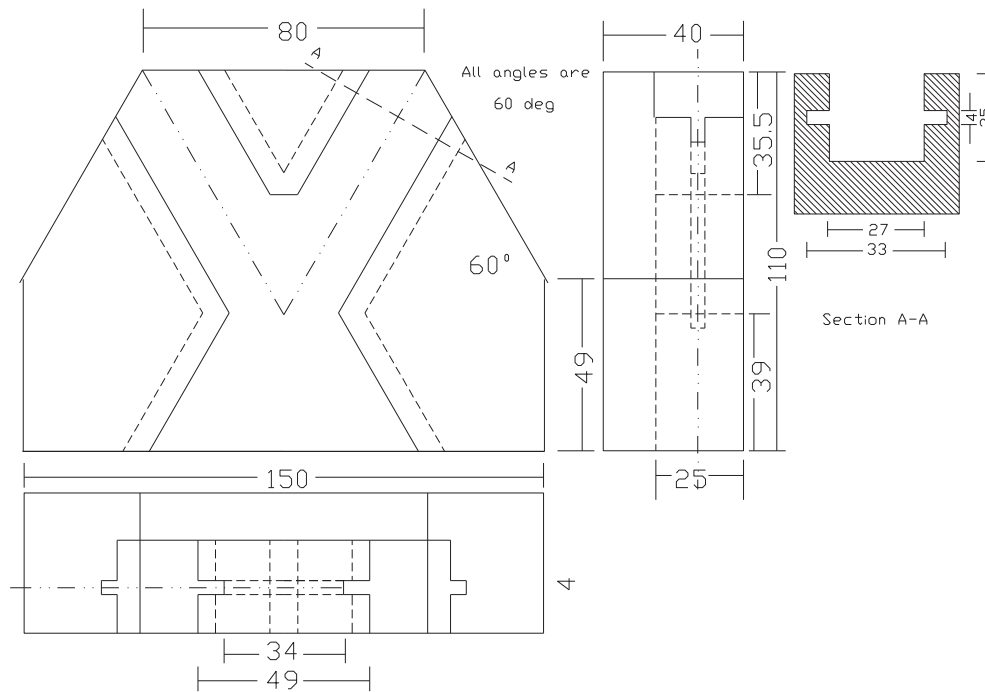


Figure B.1: Hub element; dimensions in millimetres.

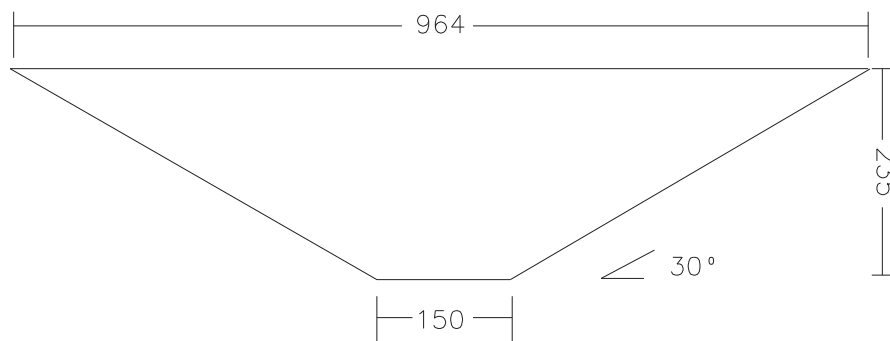


Figure B.2: Plywood base plate; dimensions in millimetres.

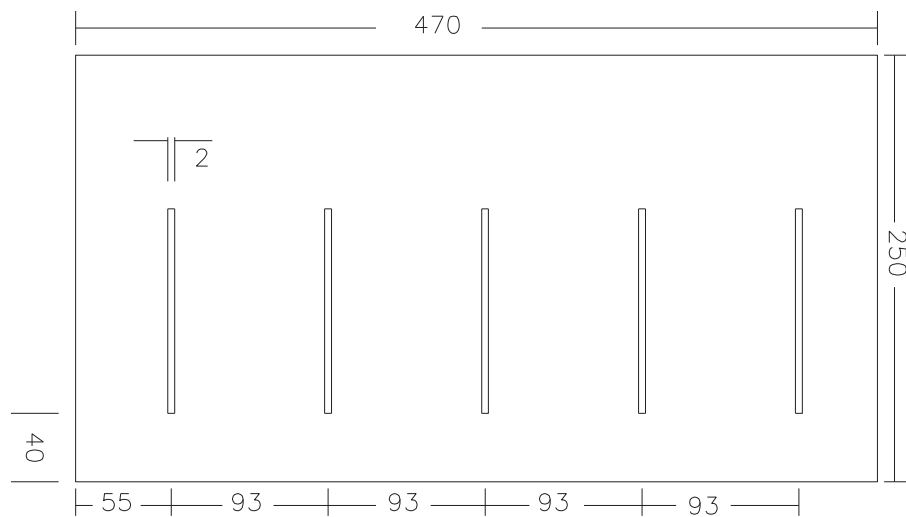


Figure B.3: Plywood side plate; dimensions in millimetres.

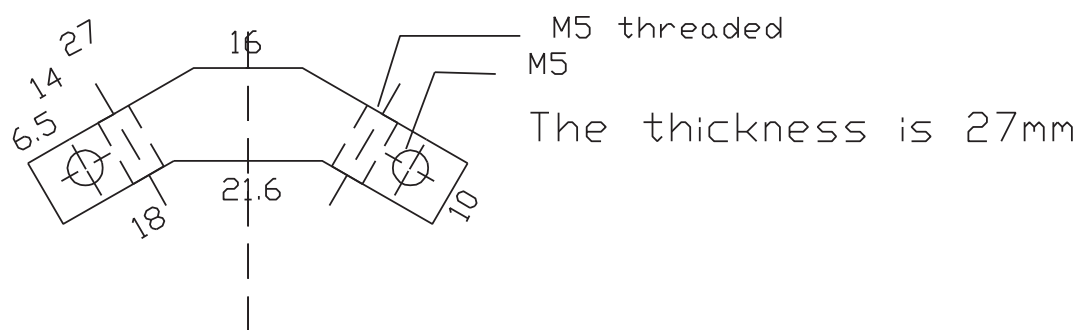


Figure B.4: Rib stop; dimensions in millimetres.

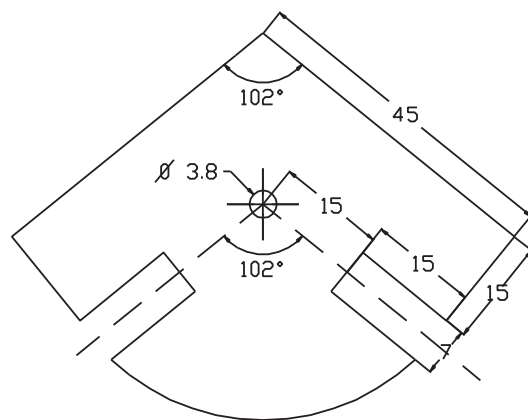


Figure B.5: End plate; dimensions in millimetres.

Bibliography

Barnes, M. R. (1982). Non-linear numerical solution methods for static and dynamic relaxation, *IL Publication*, No. 15, pp. 150-166.

Cook, R. D., Malkus, D. S. and Plesha, M. E. (1989). *Concepts and applications of finite element analysis*, Third edition, John Wiley and Sons, New York.

ESA (1992). CRTS Patent Application. 9203506 (France) and 08/035,315 (USA).

Fischer, A. (1994). Bending instabilities of thin-walled transversely curved metallic strips. Department of Engineering, University of Cambridge Report CUED/D-STRUCT/TR154.

Flügge, W. (1973). *Stresses in Shells*, Second edition, Springer Verlag, New York.

Galasko, G., Leon, J. C., Trompette, P. and Veron, P. (1997). Textile structures: a comparison of several cutting pattern methods. *International Journal of Space Structures*, Vol. 12, 9-18.

Gere, J. M. and Timoshenko, S. P. (1990). *Mechanics of materials*, Third edition. PWS-Kent Publishing Company.

Gibson, R. F. (1994). *Principles of composite material mechanics*, McGraw-Hill, New York.

Grundig, L. and Bahndorf, J. (1988). The design of wide-span roof structures using micro-computers. *Computers & Structures*, Vol. 30, No. 3, pp. 495-501.

Grundig, L. and Moncrieff, E. (1993). Formfinding of textile structures. In *Proceedings of Studiedag-Seminaire Textliestructuren Architecture Textile*, Vrije Universiteit Brussel.

Isenberg, C. (1992). *The Science of Soap Films and Soap Bubbles*, Dover Publications, London.

Kwan, A. S. K. and You, Z. (1993). User guide to Theo3, and industrial measurement system using three Zeiss ETh2 theodolites, Department of Engineering, University of Cambridge Report CUED/D-STRUCT/TR142.

Levy, R. (1996). *Structural Engineering of Microwave Antennas*, The Institute of Electrical and Electronics Engineers, New York.

Lewis, W. J. and Gosling, P. D. (1993). Stable minimal surfaces in form-finding of lightweight tension structures. *International Journal of Space Structures*, Vol. 8, 149-166.

Math Works, Inc. (1997). MATLAB Version 5, South Natick.

Oerlikon-Contraves. (1993). The technology of Inflatable Space Rigidized Structures (ISRS) long term material testing. Final report. ESTEC Contract 9126/90/NL/PP.

Przemieniecki, J. S. (1968). *Theory of Matrix Structural Analysis*, McGraw-Hill, New York.

Rits, W. J. (1996). A multipurpose deployable membrane reflector. *Esa Bulletin*, Vol. 88, pp. 66-71.

Ruze, J. (1966). Antenna tolerance theory - a review. *Proceedings IEEE*, Vol. 54, No. 4, pp. 633-640.

Schek, H. J. (1974). The force density method for form finding and computations of general networks. *Computer Method in Applied Mechanics and Engineering*. Vol. 3, pp. 115-134.

Seffen, K. A. and Pellegrino, S. (1997). Deployment of a rigid panel by tape-springs. Department of Engineering, University of Cambridge Report CUED/D-STRUCT/TR168.

Seffen, K. A., You, Z. and Pellegrino, S. (1997). Folding and deployment of curved tape springs. Department of Engineering, University of Cambridge Report, in preparation.

Seffen, K. A. and Pellegrino, S. (1999). Deployment dynamics of tape springs. In *Proceedings of the Royal Society of London*, Part A, Vol. 455, pp. 1003-1048.

Strang, G. (1980). *Linear algebra and its application*, Second edition. Academic Press New York.

Tabarrok, B. and Qin, Z. (1992). A finite element procedure for form finding of tension structures, *Transactions Canadian Society for Mechanical Engineering*. Vol. 16, No. 3 & 4. pp. 235-251.

Wakefield, D. S. (1980). Pretensioned networks supported by compression arches. PhD Dissertation. City University, London.

You, Z. and Pellegrino, S. (1994). Study of the folding and deployment aspects of a Collapsible Rib Tensioned Surface (CRTS) Antenna reflector. Department of Engineering, University of Cambridge Report CUED/D-STRUCT/TR144.